

Hydrodynamics of helical-shaped bacterial motility

Hirofumi Wada^{1,2} and Roland R. Netz²

¹*Yukawa Institute for Theoretical Physics, Kyoto University, 606-8502 Kyoto, Japan*

²*Department of Physics, Technical University Munich, 85748 Garching, Germany*

(Received 18 November 2008; revised manuscript received 4 June 2009; published 19 August 2009)

To reveal the underlying hydrodynamic mechanism for the directed propulsion of the bacterium *Spiroplasma*, we formulate a coarse-grained elastic polymer model with domains of alternating helicities along the contour. Using hydrodynamic simulations and analytic arguments, we show that the propagation of helical domain walls leads to the directed propulsion of the cell body opposite to the domain-wall traveling direction. Several key features of *Spiroplasma* motility are reproduced by our model. We in particular show that the helical pitch angle observed for *Spiroplasma meliferum*, $\psi=35^\circ$, is optimized for maximal swimming speed and energy-conversion efficiency. Our analytic theory based on the slender-body hydrodynamic approximation agrees very well with our numerical data demonstrating how the chirality switch propagating along the helical cell body is converted to a translational thrust for the cell body itself. We in detail consider thermal effects on the propulsion efficiency in the form of orientational fluctuations and conformational fluctuations of the helix shape. The body length dependence of the cell motility is studied numerically and compared to our approximate analytic theory. For fixed pitch angle $\psi=35^\circ$, the swimming speed is maximized at a ratio of cell-body length to domain length of about 2–3, which are typical values for real cells. We also propose simple analytic arguments for an enhancement of the swimming velocity with increasing solution viscosity by taking into account the effects of transient confinement of a helical cell body in a polymeric meshwork. Comparison with a generalized theory for the swimming speed of flagellated bacteria in polymeric meshworks shows that the presence of a finite-sized bacterial head gives rise to a maximal swimming speed at a finite solution viscosity, whereas in the absence of a head the swimming speed monotonically increases with increasing viscosity.

DOI: [10.1103/PhysRevE.80.021921](https://doi.org/10.1103/PhysRevE.80.021921)

PACS number(s): 87.16.Ka, 87.17.Jj, 47.63.Gd

I. INTRODUCTION

A large scale creature such as a fish owes its ability to swim solely to inertial reaction in the surrounding fluid. Fluid viscosity plays a role only in the boundary layer which only indirectly contributes by determining the magnitude of the circulation around the swimming body [1,2]. For the movement of microorganisms such as bacteria, hydrodynamics plays an entirely different role. Taylor [1] discerned that the fluid motion around a microscopic swimmer is characterized by low Reynolds numbers. The Reynolds number, Re , measures the relative importance of the fluid inertia to viscous stress, which is typically over 10^2 for a swimming fish in water. Let L be a certain length scale characterizing the size of a moving body at a typical velocity U in a fluid of density ρ and viscosity η , then the Reynolds number is given by $Re=\rho UL/\eta$. This is obtained by comparing the inertial and viscous forces appearing in the Navier-Stokes equation

$$Re = \frac{\rho \mathbf{u} \cdot \nabla \mathbf{u}}{\eta \nabla^2 \mathbf{u}} \sim \frac{\rho U^2/L}{\eta U/L^2} = \frac{\rho UL}{\eta}. \quad (1)$$

If we take typical values of an individual bacterium swimming in water, such as *Escherichia coli*, $L \sim 10^{-5}$ m and $U \sim 3 \times 10^{-5}$ m/sec, we obtain the vanishingly small value, $Re \sim 10^{-4}$, which indicates that friction typically dominates over inertia for bacterial swimming [1–5]. With such a negligibly small Re , the inertial term can be dropped, leading to the linear Stokes equation, which in the static limit reads

$$\mathbf{0} = -\nabla p + \eta \nabla^2 \mathbf{u} + \mathbf{f}, \quad (2)$$

where p is the hydrodynamic pressure determined so as to satisfy the incompressibility condition $\nabla \cdot \mathbf{u} = 0$ and \mathbf{f} is the external force distribution exerted by a moving body immersed in the fluid. As Purcell [4,5] pointed out in 1977, a geometrically reversible motion termed “reciprocal motion” does not render any net displacement due to the absence of time-dependent terms in Eq. (2). A directed propulsion is achieved for a moving body only by breaking the geometric symmetry of stroke patterns [6–10] such as by rotating helical filaments or by ciliary filaments that beat in an asymmetric fashion, as observed for various motile microorganisms in nature [1–5,11–30].

Many prokaryotes swim by rotating long helical filaments known as flagella; this mechanism is widespread among diverse groups of bacteria [31–38]. Swimming bacteria, such as *Escherichia coli*, *Salmonella typhimurium* and *Pseudomonas aeruginosa*, realize their “nonreciprocal” motion by rotating a single or several helical flagellar filaments by rotary motors embedded in the cell envelope. The helix rotational motion is converted via hydrodynamic friction into translational motion along the helix axis [3–5,10–39]. In this design, a rigid cell wall, which is composed of a protein meshwork made predominantly of peptidoglycan, and a rigid flagellum, which is a large homogeneous assembly of a single type of protein, flagellin [40], are necessary to transmit the torque generated by the motor to the filament and to the cell body.

Gliding is an alternative motility mode for nonflagellated bacteria such as cyanobacteria (blue-green algae), myxobac-

teria [41], and mycoplasma [42]. Gliding motility is realized for example when cells are in contact with a solid surface. Due to its diversity and complexity, understanding mechanisms responsible for gliding motility is at the focus of intense research in prokaryotic cell biology [43,44] and biophysics [45–48].

The remarkable functional diversity of bacteria allows for yet other propulsion modes for nonflagellated bacteria such as *Spiroplasma* [49] or cyanobacteria *Synechococcus* [50]. *Spiroplasma* are tiny helical-shaped eubacteria with a width of about 150–200 nm and typically a few microns in length [49]. They are members of the Mollicutes class (encompassing *Mycoplasma*, *Acholeplasma*, and *Spiroplasma*), which are extremely primitive and lack a rigid cell wall. *Spiroplasma* cells are wrapped by only a cholesterol-containing membrane, where cholesterol, uncommon in bacteria, renders the membrane only a small rigidity. They developed a distinct swimming strategy without the use of external flagella: they have an internal, ribbon-shaped cytoskeleton that maintains a helical shape of the cell body [51–53]. Cryo-electron tomography studies of the cytoskeletal structures have recently been reported [54,55]. It was suggested that the cytoskeleton is also responsible for the propulsion [56], but its dynamical role as an internal motor is yet to be explored. The precise propulsive mechanism remained unclear for a long time because of their minute size, but recently Shaevitz *et al.* [57] showed in a high-resolution video microscopy study that *Spiroplasma meliferum* cells swim by continuously changing their body helicity. In fact, domain walls or kinks between left- and right-handed helical regions are periodically generated at one end of the cell and propagate along the cell body giving rise to whole-cell undulation and propulsion. Although the Mollicute genome lacks analogs to any known bacterial chemotactic and motility genes, *Spiroplasma* cells exhibit chemotaxis [58,59]. Also, one particular feature of the *Spiroplasma* motility is that they swim faster in media with higher viscosity specifically in meshlike structures formed by polymers, similar to their native environment [52,57,58].

Motivated by those experimental observations, we develop in this paper a simple model based on an elastic filament that consists of unidirectionally moving domain walls between sections of left- and right-handed helicity. Using hydrodynamic simulations as well as analytic calculations based on slender-body hydrodynamics [60,61], we reproduce several key features of *Spiroplasma* motility observed experimentally: (i) the cell itself moves in a direction opposite to the kink propagation, (ii) the linear swimming velocity is proportional to the kink velocity, with a proportionality constant in fair agreement with experiments [52,57], (iii) the center-of-mass motion follows a helical trajectory with a pitch close to the pitch of the cell body, (iv) the optimal hydrodynamic propulsion efficiency is obtained at a cell-body pitch angle of around $\psi \approx 35^\circ$ identical to the actual pitch of *Spiroplasma* of about $\psi \approx 35^\circ$, and (v) for the optimal pitch angle, the largest swimming speed is obtained for a ratio of cell length to domain length of around 2–3, close to values typically observed for real cells.

Enhancement of *Spiroplasma* motility in viscoelastic materials is considered within a simple slender-body hydrody-

namics approach originally proposed by Magariyama *et al.* [62,66] that takes into account the effects of anisotropic friction due to the presence of a gel-like polymer network in the surrounding fluid. Comparison with a generalized theory for the swimming speed of flagellated bacteria in polymeric meshworks shows that the presence of a finite-sized bacterial head gives rise to a maximal swimming speed at a finite solution viscosity, while the swimming speed monotonically increases with viscosity for helical shaped bacteria without a head. These results are consistent with previous experimental observations both for flagellated and helical-shaped bacteria [52,57,63–66]. We also consider thermal effects in the form of orientational random fluctuations and conformational shape fluctuations on the propulsion speed and find that for stiff enough cell bodies these effects are rather small.

A brief report of our results has recently been published [67]. The present paper presents more details, data on length and fluctuation effects, and an extended analysis of the swimming speed of helical swimmers in anisotropic friction media including the effects of the presence of a head (such as relevant for flagellated bacteria). The paper is organized as follows. In the next section, we set up our elastic filament model that incorporates the propagating chirality domain walls. The hydrodynamic equations are presented and the numerical simulation procedure is briefly described. In Sec. III, the swimming behavior of helical filaments obtained from the hydrodynamic simulations is described in detail, which includes geometrical properties of the swimming trajectory, the swimming velocity, and the energy-conversion efficiency as a function of the kink (i.e., the domain wall) velocity. In Sec. IV, analytic arguments based on slender-body hydrodynamics theory are presented in order to clarify the physical mechanism of *Spiroplasma* propulsion. The analytic predictions are shown to agree well with corresponding numerical data (and experimental results). We show that the observed *Spiroplasma* cell shape is designed to achieve optimal swimming speed and efficiency. Effects of Brownian motion are considered in Sec. V. The mean-square displacement of the center of mass of a moving helix is monitored and its long-time behavior is explained by an effective Langevin equation with the aid of knowledge obtained in Secs. III and IV. In Sec. VI, effects of fluid viscosity on the swimming motility are discussed within a simple analytic model and compared favorably with experimental data [52]. The final section summarizes our main results obtained in this paper. A comprehensive analytic theory for bacterial swimming motility based on slender-body hydrodynamics theory, including helical-shaped filamentous cells as well as externally flagellated cells in a fluid of anisotropic viscosity, is presented in Appendix A. Appendix B links our simplified analysis for a rotating rigid helix to Lighthill's Stokeslet calculation [3]. The fundamental kinematic equations of a slender elastic rod are summarized in Appendix C, followed by details on our numerical simulation method in Appendix D.

II. MODEL

A. Elastic energy of an isotropic rod

The *Spiroplasma meliferum* cell is a slender object; its total arclength L , typically $L \sim 5\text{--}10 \mu\text{m}$, is much larger

than its diameter $a \sim 100\text{--}200$ nm [51,53]. The cell may thus be modeled as an isotropic elastic rod and the rod shape is described by the position vector of the centerline of the rod $\mathbf{r}(s)$, which is parametrized by the arclength s measured from one end. (Electron micrography has demonstrated that a *Spiroplasma melliferum* cell is in fact ribbon-shaped, but this anisotropy of the cross section might change our results only quantitatively and is not considered in this study.) Within our continuum mechanics treatment, kink-pair propagation is modeled by prescribed space-time-dependent intrinsic curvature and torsion profiles. The elastic energy for the dynamic helical rod is thus given by

$$E_{\Omega}(t) = \frac{A}{2} \int_0^L ds \Omega_1^2 + \frac{A}{2} \int_0^L ds (\Omega_2 - \Omega_2^0)^2 + \frac{C}{2} \int_0^L ds [\Omega_3 - \Omega_3^0(s,t)]^2, \quad (3)$$

where A and C are, respectively, the bending and twisting moduli [68]. $\Omega = (\Omega_1, \Omega_2, \Omega_3)$ is the strain rate vector; $\kappa = (\Omega_1^2 + \Omega_2^2)^{1/2}$ gives the local curvature and Ω_3 is the twist density. For a uniform helix, we set $\Omega_1^0 = 0$, $\Omega_2^0 = \kappa_0$, and $\Omega_3^0 = \tau_0$ (see also Appendix D), where κ_0 and τ_0 are the intrinsic curvature and torsion related to the helix radius R and pitch P as

$$\kappa_0 = \frac{4\pi^2 R}{P^2 + 4\pi^2 R^2} \quad \text{and} \quad \tau_0 = \frac{2\pi P}{P^2 + 4\pi^2 R^2}. \quad (4)$$

In an alternative parametrization the helical geometry is specified by the pitch angle ψ , related to pitch P and radius R via

$$\tan \psi = \frac{2\pi R}{P}, \quad (5)$$

and the contour length per helical turn, $\ell = (P^2 + 4\pi^2 R^2)^{1/2}$ (see Fig. 1). A further relation is given by

$$\kappa_0 = \frac{2\pi}{\ell} \sin \psi \quad \text{and} \quad \tau_0 = \frac{2\pi}{\ell} \cos \psi. \quad (6)$$

B. Modeling of kink-pair propagation

According to experimental observation, kinks are always generated at the same end and travel down the cell body at constant speed [57]. Time spans between two consecutive kinks, i.e., between kinks within a pair, τ_k , is observed to be approximately Gaussian distributed with a mean of $\bar{\tau}_k \approx 0.26$ s. The kink (or domain wall) velocity along the cell body was measured to be $V_0 \approx 10.5 \pm 0.3$ $\mu\text{m/s}$, giving an average domain size $\bar{D} \approx V_0 \bar{\tau}_k \approx 2.7$ μm and thus $\bar{D}/L \approx 0.5$ for a cell of typical length $L \approx 5$ μm long. The time span between kink pairs during which the cell remains straight and thus does not move except Brownian motion, τ_w , was reported to be exponentially distributed starting from $\tau_w = 0$ s and decaying with a time constant of 1 s. We set $\tau_w = 0$ throughout this study, because the period during which the filament consists of a homogeneous helix is of minor

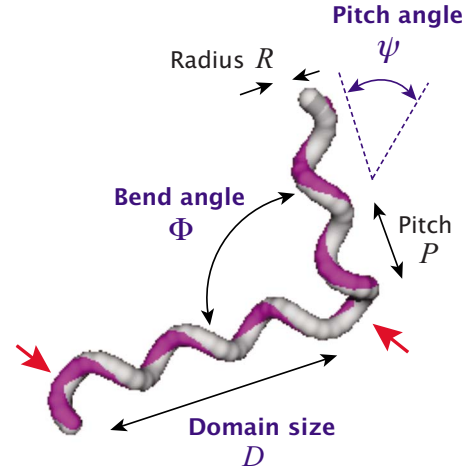


FIG. 1. (Color online) Geometry of a bistable helix with two kinks (i.e., domain walls between different chiralities), which are indicated by arrows. Bending of the helical axes by an angle Φ is present at the domain wall between left- and right-handed helical sections.

importance for its swimming properties. The time scale τ_w might be relevant for chemotactic properties, as discussed in Ref. [57].

The change in helicity is driven by the internal ribbon-shaped cytoskeletal motion whose microscopic mechanism is not yet well understood [51–54]. The outer membrane tube that defines the helical shape of the cell is believed to respond elastically to conformational changes in the cytoskeleton. In our elastic rod model, the propagation of a pair of kinks or domain walls between left- and right-handed helical sections is described by a square-wave-like profile of the intrinsic twist:

$$\Omega_3^0 = \tau_0 [1 + 2\{\theta(s - V_0 t - D, L) - \theta(s - V_0 t, L)\}], \quad (7)$$

which is defined only for $0 \leq s \leq L$. The domain size D , within which $\Omega_3^0 = -\tau_0$, fluctuates from one period to the other around the average value \bar{D} . The step function $\theta(z)$ is defined as $\theta(z) = 1$ for $z > 0$ and $\theta(z) = 0$ for $z < 0$. The kink or domain-wall propagation in our model mimics the experimental observation. A schematic diagram of the kink-pair propagation in one period is shown in Fig. 2(a). The actual domain length $d(t)$ along the contour (in which $\Omega_3^0 = -\tau_0$) thus changes in time within one actuation period $T_0 = (L + D)/V_0$ that also fluctuates from one period to the other due to D and is given by

$$d(t) = \begin{cases} V_0 t & (0 \leq t \leq D/V_0) \\ D & (D/V_0 \leq t \leq L/V_0) \\ (D + L) - V_0 t & (L/V_0 \leq t \leq T_0). \end{cases} \quad (8)$$

A typical time course of $d(t)$ taken from our simulation is displayed in Fig. 2(b) as an example.

C. Geometric properties of bistable helices

When a right- and a left-handed helix, whose pitch angles are ψ_1 and ψ_2 (taken positive irrespective of its chirality), are

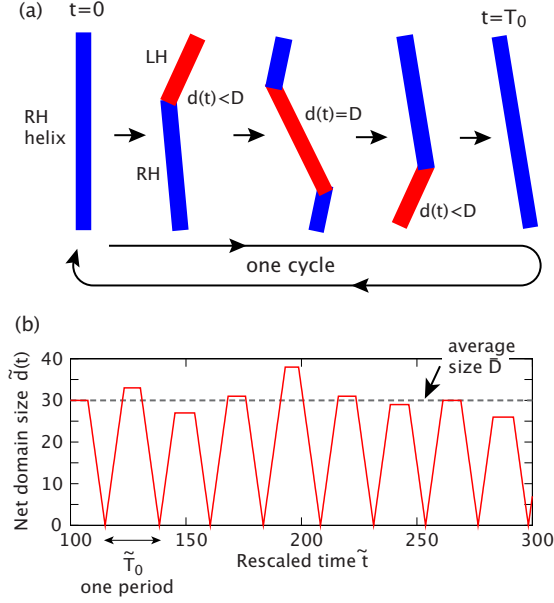


FIG. 2. (Color online) (a) Schematic diagram of the kink-pair propagation for one complete cycle of period T_0 . Initially the cell takes a right-handed (RH) helix (indicated with blue) and the left-handed (LH) helical section (indicated with red) nucleates at the top and travels down along the cell at constant speed V_0 . The net domain length (along the contour) reaches its maximum D , and then decreases again, leading finally to the original RH helical shape. The cell repeats this cycle and propels itself upward. (b) An example of the time course of the net domain length $\tilde{d}(t) = d(t)/a$ taken from an actual simulation run. The maximum domain size D fluctuates around its average $\bar{D} = 30a$ according to a Gaussian distribution. See text.

linked together, a bend with angle Φ at the junction (defined in Fig. 1) appears and is in the absence of external stress given by [57,69,70]

$$\Phi = \pi - \psi_1 - \psi_2. \quad (9)$$

The bend angles for *Spiroplasma melleiferum*, which were found almost constant over all cells studied, have been measured to be $\Phi = 111^\circ \pm 9^\circ$. Independent measurements of the two pitch angles yielded $\psi_1 = 34.6^\circ \pm 0.5^\circ$ and $\psi_2 = 35.1^\circ \pm 0.5^\circ$, which are indeed consistent with the above geometric assumption, Eq. (9) [57]. In line with these experimental facts, we set in this paper $\psi_1 = \psi_2 = \psi$. Equation (9) thus reduces to $\Phi = \pi - 2\psi$.

D. Simulation method

In our numerical simulations the filament is modeled as a chain of $N+1$ connected spheres of diameter a . The total elastic energy $E_{tot} = E_\Omega + E_{st}$ includes a stretching energy that ensures the connectivity of the chain and is given by

$$E_{st} = \frac{K}{2} \sum_{j=1}^N (|\mathbf{r}_{j+1} - \mathbf{r}_j| - a)^2, \quad (10)$$

where \mathbf{r}_j is the j th sphere position. The stretching modulus is set to $K = 16A/a^2$, which corresponds to an isotropic rod and

is large enough to limit stretching of the bonds to a negligible level for the range of values of the bending modulus A studied in this paper. The local elastic force, \mathbf{F}_i , and torque about the local tangent, T_i , acting on the i th sphere are calculated from E_{tot} using a variational method [71–73]. Our simulation method is described in detail in Appendix D. For the viscous motion of a sphere in a Stokes fluid, inertial effects are negligible, which leads to the coupled position Langevin equations given by

$$\frac{\partial}{\partial t} \mathbf{r}_i = \sum_{j=1}^{N+1} \boldsymbol{\mu}_{ij} \cdot \mathbf{F}_j + \boldsymbol{\xi}_i(t), \quad (11)$$

$$\frac{\partial}{\partial t} \phi_i = \mu_r T_i + \Xi_i(t), \quad (12)$$

where the variable ϕ_i is the spinning angle of the bond vector $\mathbf{r}_{i+1} - \mathbf{r}_i$; see also Appendix C. Hydrodynamic interactions between two spheres i and j are included via the Rotne-Prager mobility tensor

$$\boldsymbol{\mu}_{ij} = \frac{1}{8\pi\eta r_{ij}} \left[\mathbf{1} + \frac{\mathbf{r}_{ij}\mathbf{r}_{ij}}{r_{ij}^2} + \frac{a^2}{2r_{ij}^2} \left(\frac{\mathbf{1}}{3} - \frac{\mathbf{r}_{ij}\mathbf{r}_{ij}}{r_{ij}^2} \right) \right], \quad (13)$$

for nonoverlapping spheres, i.e., $r_{ij} > a$ [74,75] and for overlapping spheres $r_{ij} < a$ [76]

$$\boldsymbol{\mu}_{ij} = \frac{1}{8\pi\eta a} \left[\left(\frac{8}{3} - \frac{3r_{ij}}{2a} \right) \mathbf{1} + \frac{\mathbf{r}_{ij}\mathbf{r}_{ij}}{2ar_{ij}} \right], \quad (14)$$

where η is the solvent viscosity. This large-distance expansion becomes inaccurate for touching spheres, which is of no concern for the present study since it is the long-ranged part of the hydrodynamic interactions that dominates the propulsion behavior. For the translational and rotational self-mobilities of the spherical monomers we use $\boldsymbol{\mu}_{ii} = \mathbf{1}/(3\pi\eta a) \equiv \mu_0 \mathbf{1}$ and $\mu_r = 1/(\pi\eta a^3)$ [77]. The random displacements $\boldsymbol{\xi}_i(t)$ and $\Xi_i(t)$ in Eqs. (11) and (12) model the coupling to a heat bath and satisfy the fluctuation-dissipation relations $\langle \boldsymbol{\xi}_i(t) \boldsymbol{\xi}_j(t') \rangle = 2k_B T \boldsymbol{\mu}_{ij} \delta(t-t')$ and $\langle \Xi_i(t) \Xi_j(t') \rangle = 2k_B T \mu_r \delta(t-t')$, which are implemented numerically by Cholesky factorization [74].

The intrinsic twist, given in Eq. (7) in the continuum description, is discretized as

$$\Omega_{3,j}^0(t) = \frac{1}{a} \int_{(j-1)a}^{ja} \Omega_3^0(s,t) ds, \quad (15)$$

so that $\Omega_{3,j}^0(t)$ located at the domain front changes continuously and linearly in time to ensure a smooth propagation of the domain walls or kinks. A precise input power supplied by this domain-wall propagation cannot be *a priori* evaluated in an analytic way and is measured numerically by making use of the fact that the power fueled to the filament is strictly equal to the total power dissipated viscously into the surrounding fluid in our Stokesian simulations.

For the numerical integrations we discretize the Langevin Eqs. (11) and (12) with a time step Δ . The number of spheres is changed in the range $L/a = N = 40-100$ to study systematically the length dependence of the cell motility. On the other hand, we fix the length for one helical turn to $\ell = 10a$. The

number of turns per filament is thus 4–10, as frequently observed in experiments [49,51,52,57]. For the finite-temperature simulations we rescale all parameters by the sphere diameter a , the thermal energy $k_B T$, and the unit time $a^2/(\mu_0 k_B T)$, leading to dimensionless parameters $\tilde{\Delta}^{(T)} = \Delta k_B T \mu_0 / a^2$ and $\tilde{V}_0^{(T)} = V_0 a / (\mu_0 k_B T)$. For the zero-temperature simulations, we omit the random-force terms in Eqs. (11) and (12) and use the rescaled parameters $\tilde{\Delta} = \Delta \mu_0 A / \ell^3$ and $\tilde{V}_0 = V_0 \ell^3 / (\mu_0 A a)$. For sufficient numerical accuracy we choose a time step $\tilde{\Delta} = \tilde{\Delta}^{(T)} = 0.000\ 02$. Output values are calculated every 10^3 – 10^4 steps, total simulation times are 10^7 – 10^8 steps. The domain size D is chosen randomly for each kink pair from a Gaussian distribution with mean $\bar{D} = 30a$ and dispersion $\Delta_{2D} \approx 4a^2$. While the rescaled domain velocity, \tilde{V}_0 or $\tilde{V}_0^{(T)}$, is varied in the range of 1–10 (see for example the data in Fig. 7 below), most of the data are obtained for $\tilde{V}_0 = \tilde{V}_0^{(T)} = 4.0$. We set the twist-bend rigidity ratio to $C/A = 1$, i.e., the Poisson ratio is zero, which is valid for an isotropic elastic rod [68]. The bend and twist rigidities A and C for a *Spiroplasma* cell are not well characterized experimentally. In the main part of our study, we use $\tilde{A} = 10^3$ for zero-temperature simulations and $L_p/a = A/(k_B T a) = 10^3$ for finite-temperature simulations, which corresponds to a bending persistence length $L_p = A/k_B T = 10^3 a \approx 10^2 \mu\text{m}$ for $a \approx 10^2 \text{ nm}$, and thus greatly exceeds the body length $L \approx 5$ – $10 \mu\text{m}$, i.e., $L_p/L > 10$. For large stiffness, the mechanics of the cell is mainly dictated by a balance between elastic deformation and active domain-wall propagation. Random thermal noise is less important and only determines the long-time swimming kinematics and mechanics of *Spiroplasma*. Thus, for improved data accuracy, we perform zero-temperature simulations in the main part of this study. Nevertheless, thermal fluctuations affect cell motility in two ways. (1) For sufficiently long times, swimming trajectories are affected by Brownian motion through the randomization of the propulsion direction due to thermal noise. (2) Brownian random bending of the cell body softens the cell and thereby influences the motion and propulsion of the cell. These issues will be studied in Sec. V, where we systematically change the magnitude of A to study effects of cell stiffness on *Spiroplasma* swimming properties in finite-temperature simulations.

III. RESULTS

A. Swimming pattern and trajectories

Selected snapshots of a single swimming cell with a pitch angle $\psi = 35^\circ$, cell length $N = 61$, and rescaled domain velocity $\tilde{V}_0 = 4.0$ are shown in Fig. 3. In this panel, the filament swims from right to left as the pair of domain walls (indicated by the arrows) travels down along the filament contour. This swimming motion is explicitly visualized by the center-of-mass trajectory $\mathbf{R}_c(t) = \sum_{j=1}^{N+1} \mathbf{r}_j(t) / (N+1)$ in Fig. 4, which traces fluctuating straight trajectories for $\psi = 30^\circ$ and 35° , and a rather winding path for $\psi = 45^\circ$. The inset of Fig. 4 is a close-up view of a trajectory for a cell of pitch angle ψ

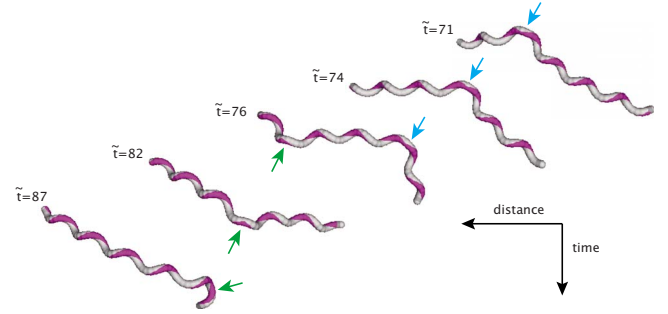


FIG. 3. (Color online) Snapshots of the swimming bistable helix for $N = 61$ and pitch angle $\psi = 35^\circ$. Moving domain walls or kinks are indicated by arrows. Time and traveling distance are not scaled properly in this panel. Net filament translation over one period $\tilde{T}_0 \approx 22.5$ is about $8a$. Temperature is set to zero, the rescaled bending energy is $\tilde{A} = 10^3$, and the rescaled kink velocity is $\tilde{V}_0 = 4.0$.

$= 35^\circ$ during the time range $20 \leq \tilde{t} \leq 80$, which roughly corresponds to two and half cycles, $\approx 2.5T_0$. One can discern a zigzag (or helical) swimming trajectory, which is consistent with experimental observations [57].

B. Modes of chirality transformation

For the helicity transformation, two different kinematical modes are in principle possible; see Fig. 5. The first one is a “crankshafting” mode, in which one of the two helical sections pivots about the other, and the other is a “speedometer-cable” mode where both helical sections rotate about their own axes [70]. On the scaling level, the dissipations for crankshafting and speedometer-cable motion are estimated, respectively, as

$$P_{cr} \sim \zeta_H \omega^2 h^3 \sin^2 \Phi \quad \text{and} \quad P_{sp} \sim \zeta_H R^2 \omega^2 L, \quad (16)$$

where ω is the axial rotation rate, R is the helix radius, h denotes the length of the moving helical section [projected

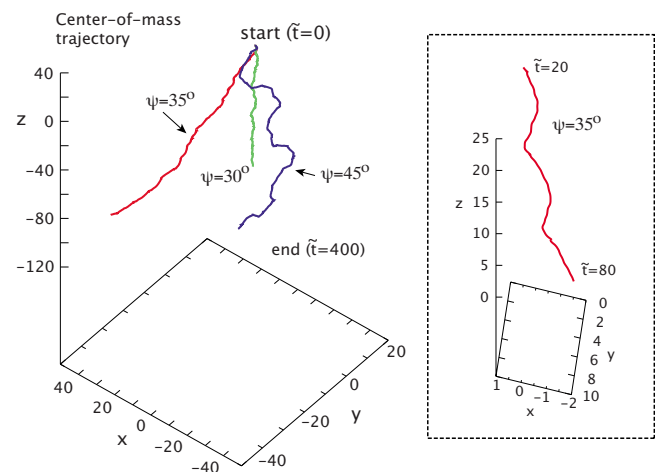


FIG. 4. (Color online) Center-of-mass trajectories for various pitch angles ψ , for cell length $N = 61$, bending energy $\tilde{A} = 10^3$ and domain speed $\tilde{V}_0 = 4.0$, obtained for $0 \leq \tilde{t} \leq 400$ in zero-temperature simulations. Inset: close-up view of the center-of-mass trajectory for $20 \leq \tilde{t} \leq 80$ (for pitch angle $\psi = 35^\circ$).

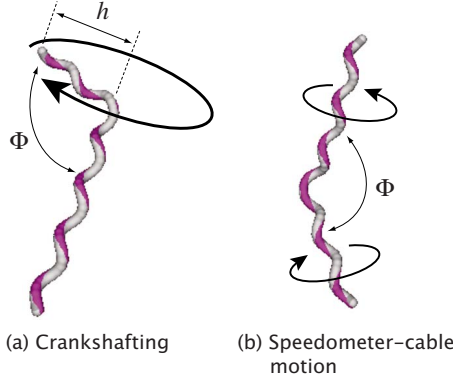


FIG. 5. (Color online) Two geometrically possible motion modes for a helix as it transforms its chirality: (a) crankshafting motion in which one of the two helical sections pivots about the other and (b) speedometer-cable motion where both helical sections rotate about their own axes.

on the helical axis, see Fig. 5(a)] and ζ_H is the helical friction coefficient per unit length (whose specific value is not relevant for the present purpose). According to the minimum dissipation theorem for Stokes flow [78], crankshafting motion dominates for $P_{sp} > P_{cr}$ and thus for $h^3 \sin^2(2\psi) < R^2 L$. Considering $h \approx d(t) \cos \psi$, the above condition is rewritten as $d(t) < [R^2 L / (\sin \psi \tan \psi)]^{1/3} \approx 1.4 R^{2/3} L^{1/3}$ for typical pitch angles $\psi = 20^\circ - 50^\circ$ studied here, and it thus turns out that this window is quite limited to only beginning and ending of a domain-wall propagation for our parameter set and for typical experimental situations. Indeed, speedometer-cable motion is the predominant mode of motion observed experimentally [57] and in the simulations [67]. Since the chirality transformation requires the generation of twist, in the speedometer-cable motion, both helical sections rotate about their own axes in *opposite* directions. The fact that the rotational directions are opposite for helices with opposite chirality is central for the understanding of the propulsion mechanism of *Spiroplasma*, because both helical parts generate thrust in the *same* direction. This idea is later corroborated by developing an analytic argument based on slender-body hydrodynamic theory in Sec. IV.

C. Swimming speed and efficiency

To quantify swimming properties of our active helical filaments, we examine the (time-dependent) mean velocity defined as

$$v(t) = \frac{|\mathbf{R}_c(t) - \mathbf{R}_c(0)|}{t}, \quad (17)$$

whose convergence within the simulation time is checked numerically in Fig. 6(a); the mean velocity is taken as $V = \lim_{t \rightarrow \infty} v(t)$. However, the swimming trajectory of the filament ceases to be unidirectional after a sufficiently long time due to the fluctuations of the domain size (even without any thermal fluctuations) for larger ψ . The linear velocity V by itself is thus not enough to characterize the swimming motion of the helix for large ψ . We therefore also directly look at the velocity along the contour of the \mathbf{R}_c -trajectory:

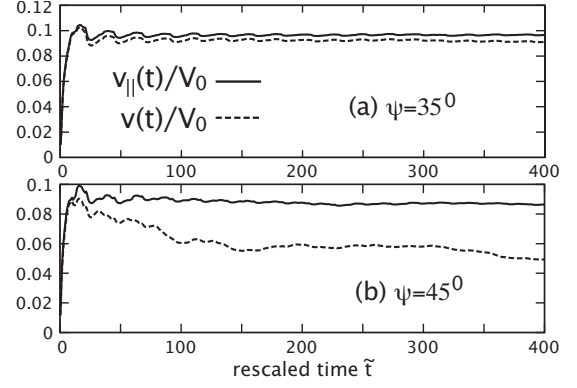


FIG. 6. Net swimming velocity (rescaled by the kink velocity V_0), $v(t)/V_0$ (broken line), and the tangential swimming velocity (rescaled by the kink velocity V_0), $v_{||}(t)/V_0$ (solid line), plotted as a function of rescaled time \tilde{t} for a pitch angle (a) $\psi = 35^\circ$ and (b) $\psi = 45^\circ$, obtained in zero-temperature simulations. The monomer number is $N = 61$, $\tilde{A} = 10^3$, and $\tilde{V}_0 = 4.0$ in (a) and (b).

$$v_{||}(t) = \frac{1}{t} \int_0^t dt' \sqrt{1 + [\dot{\mathbf{R}}_c(t')]^2}, \quad (18)$$

where $\dot{\mathbf{R}}_c(t) = d\mathbf{R}_c/dt$. This quantity shows a better convergence than $v(t)$ for larger pitch angle [see Fig. 6(b)] and the convergent value is taken as “the tangential velocity” along the trajectory, i.e., $V_{||} = \lim_{t \rightarrow \infty} v_{||}(t)$.

We show the mean velocity \tilde{V} and the tangential velocity along the contour $\tilde{V}_{||}$ in Fig. 7(a) as a function of the domain velocity \tilde{V}_0 for a pitch $\psi = 35^\circ$, domain size $\tilde{D} = 30a$, and monomer number $N = 61$. We extract from the data linear relations $\tilde{V} \approx 0.082 \tilde{V}_0$ and $\tilde{V}_{||} \approx 0.092 \tilde{V}_0$. For standard medium used in the experiments as a solvent, the viscosity is $\eta_s \approx 1.147$ cP, and assuming $a \approx 200$ nm, we obtain $V_0 = \tilde{V}_0 a / \tau \approx 10 \tilde{V}_0 [\mu\text{m/s}]$. Experimental reports on V_0 range from $10 \mu\text{m/s}$ to $40 \mu\text{m/s}$ [52,57], thus $\tilde{V}_0 \approx 1-4$ denotes the experimentally relevant range of values. The ratio of mean swimming velocity and domain-wall velocity projected along the helical axis, $V/(V_0 \cos \psi)$, extracted from the simulation data for $\psi = 35^\circ$ is $V/(V_0 \cos \psi) \approx 0.10$. A previous comprehensive experimental study reported a value around 0.05 [52], but the data from the latest experiment give a value around 0.3 [57]. Both are optical measurements for tiny bacteria, and the largest error is obtained for the kink or domain-wall velocity V_0 , while the cell’s swimming speed is consistently reported around $V \approx 1-3 \mu\text{m/s}$ in both measurements. The large experimental uncertainty present at this stage suggests considering the agreement between our simulation results and the existing experimental values as satisfactory.

The domain motion locally feeds power into the system, which viscously dissipates into the surrounding fluid. The total dissipated power is numerically calculated as

$$P_{dis} = \lim_{T \rightarrow \infty} \frac{1}{T} \int_0^T \sum_{j=1}^N [\mathbf{F}_j \cdot \mathbf{v}_j + T_j \omega_j] dt, \quad (19)$$

where $\mathbf{v}_j = \partial \mathbf{r}_j / \partial t$ and $\omega_j = \partial \phi_j / \partial t$ are, respectively, the translational and rotational velocities of sphere j . To estimate the

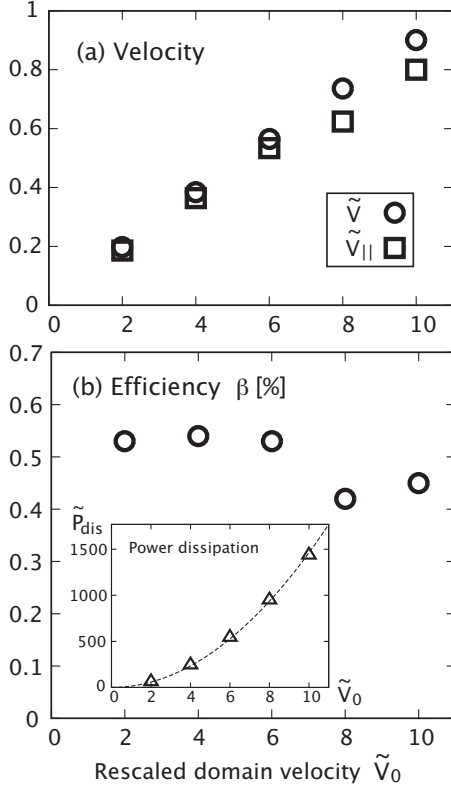


FIG. 7. (a) Rescaled mean and tangential swimming velocities, $\tilde{V}=V\ell^3/(\mu_0 Aa)$ and $\tilde{V}_{||}=V_{||}\ell^3/(\mu_0 Aa)$, as a function of the kink velocity \tilde{V}_0 for $N=61$ and fixed pitch angle $\psi=35^\circ$. (b) Efficiency $\beta = \tilde{P}_s/\tilde{P}_{dis} = (2/3)N\tilde{V}^2/[\ln(4N)-3/2]\tilde{P}_{dis}$ as a function of \tilde{V}_0 for $N=61$ and $\psi=35^\circ$. The inset shows the rescaled dissipated power, $\tilde{P}_{dis}=P_{dis}\ell^6\mu_0^{-1}/(Aa)^2$, as a function of \tilde{V}_0 . The broken line is a quadratic fit. All data were obtained in zero-temperature simulations.

hydrodynamic power-conversion efficiency of the moving helix, we relate the total dissipated power P_{dis} [shown in the inset of Fig. 7(b)] to the power expended to move a corresponding straight filament of length $L=aN$ at net velocity V , which is

$$P_s = \frac{2\pi\eta LV^2}{\ln(4L/a) - 3/2}, \quad (20)$$

in line with previous definitions [3,8,9,27]. The ratio $\beta = P_s/P_{dis}$ defines our efficiency, which is plotted as a function of V_0 in Fig. 7(b). The efficiency β shows a weak dependence on V_0 and seems to converge for decreasing V_0 around $\beta \approx 0.5$ [%], thus much less than efficiencies of flagellated microswimmers [8,23,26,27,79].

IV. ANALYTIC MODEL FOR HELIX PROPULSION

A. Translation of a rotating rigid helix

To develop a theory for *Spiroplasma* propulsion, we first calculate the propulsion of a single rigid helix that rotates at frequency ω by an externally applied torque; see Fig. 8(a). Taking $\hat{\mathbf{z}}$ as the helical axis, the helix centerline is given by

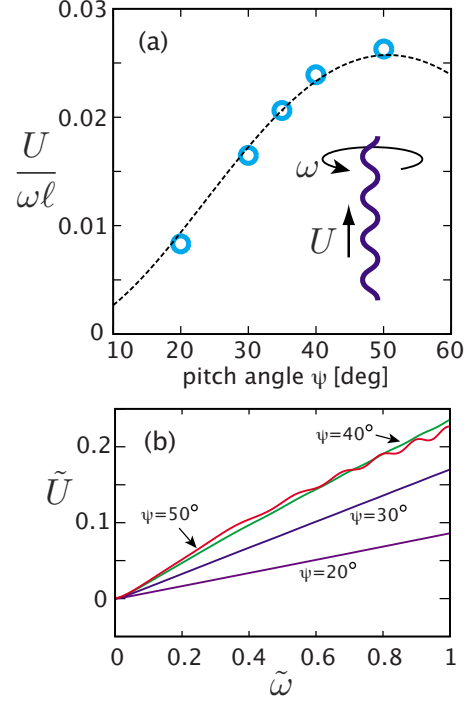


FIG. 8. (Color online) (a) Reduced translational velocity, $U/(\ell\omega)$, for a stiff (but still elastic) helix that is forced to rotate at frequency ω , obtained from the full hydrodynamic simulations, plotted as a function of pitch angle ψ . The broken line is the best fit of Eq. (25) to the data with $\xi=1.55$. (b) Rescaled translational velocity along $\hat{\mathbf{z}}$, \tilde{U} as a function of the rescaled rotating frequency $\tilde{\omega}$ for various pitch angles ψ indicated in the figure, from which the value of $U/(\ell\omega)$ is extracted. All data were obtained in zero-temperature simulations.

$$\mathbf{r}(s,t) = \begin{bmatrix} R \cos(2\pi s/\ell + \omega t) \\ R \sin(2\pi s/\ell + \omega t) \\ bs + Ut \end{bmatrix}, \quad (21)$$

where $2\pi R/\ell = \sin \psi$, $b = \cos \psi$, and U is the propulsion velocity to be determined. If we assume the helix to be composed of small cylinders, the slender-body theory gives a force per length acting on the helix, \mathbf{f} , as

$$\mathbf{f} = \zeta_{\perp}[\mathbf{u} - (\mathbf{t} \cdot \mathbf{u})\mathbf{t}] + \zeta_{||}(\mathbf{t} \cdot \mathbf{u})\mathbf{t}, \quad (22)$$

where $\mathbf{t} = \partial\mathbf{r}/\partial s$ is the local tangent, $\mathbf{u} = \partial\mathbf{r}/\partial t$ is the velocity, and ζ_{\perp} and $\zeta_{||}$ are the perpendicular and parallel friction coefficients of the cylinder segments [56,61,80]. (Approximate expressions valid for a helix are discussed later on.) Using the fact that the total force on the translationally unconstrained helix is zero, $\int_0^L \mathbf{f}(s)ds = 0$ and decomposing \mathbf{u} as $\mathbf{u} = U\hat{\mathbf{z}} + \mathbf{u}_{\perp}$, we obtain

$$\begin{aligned} & \int_0^L ds [\zeta_{\perp} + (\zeta_{||} - \zeta_{\perp})(\mathbf{t} \cdot \hat{\mathbf{z}})^2] U \\ & = -(\zeta_{||} - \zeta_{\perp}) \int_0^L ds (\mathbf{t} \cdot \hat{\mathbf{z}})(\mathbf{t} \cdot \mathbf{u}_{\perp}). \end{aligned} \quad (23)$$

Plugging Eq. (21) into Eq. (23) and solving in terms of U , we obtain the translational velocity

$$U = S\ell\omega, \quad (24)$$

where S is a helix shape-dependent coefficient given by

$$S(\psi) = \frac{(\xi - 1)\sin^2 \psi \cos \psi}{2\pi[1 + (\xi - 1)\sin^2 \psi]}, \quad (25)$$

where $\xi = \zeta_{\perp} / \zeta_{\parallel}$ is the ratio of the perpendicular friction coefficient to the parallel friction coefficient. In the free-draining limit where long-ranged effects mediated by the hydrodynamic flow are neglected, i.e., $\xi = 1$, we have $U = 0$ as expected. For a slender rod of length L and of radius a , ξ is generally larger than unity and approaches $\xi = 2$ in the limit of $L/a \rightarrow \infty$. This limit is, however, not attained for a helix of finite length and of finite cross section. The ratio ξ may thus be treated as a fitting parameter (confined within $1 < \xi \leq 2$) to best account for our numerical data obtained from full Stokesian simulations. We note that one recovers Eq. (25) with $\xi = 2$ by taking the singular limit, i.e., vanishing regularization cutoff (which is equivalent to the $L/a \rightarrow \infty$ limit) in the classical Lighthill's Stokeslet theory. This is shown in detail in Appendix D.

To check the validity of Eq. (25), it is compared to numerical data for an elastic helix obtained from our simulation including full hydrodynamic interactions without thermal noise. In those simulations, the helix is forced to rotate at one end at frequency ω by an externally applied torque and thus propels along its helical axis with a velocity U . The obtained numerical value of $U/(\ell\omega)$ is plotted in Fig. 8(a) as a function of pitch angle ψ . Good agreement between the data and Eq. (25) is obtained for a fit value $\xi = 1.55$.

The local friction coefficients of a helical rod, ζ_{\parallel} and ζ_{\perp} , were first suggested by Gray and Hancock [11] and later improved by Lighthill [3]. In Lighthill's argument, a helical arrangement of Stokeslets was taken into account for an infinitely stiff and long helix, and Stokes doublets were adjusted to locally fulfill the no-slip boundary condition for an approximate straight cylinder shape. The calculation yielded [3]

$$\zeta_{\parallel} = \frac{\pi\eta}{\ln(4q/a)} \quad \text{and} \quad \zeta_{\perp} = \frac{4\pi\eta}{2 \ln(4q/a) + 1}, \quad (26)$$

where q may be seen as an effective length of cylindrical segments and was taken as $q \approx 0.09P$ (remember that $P = \ell \cos \psi$ is the helix pitch). For the parameters in Fig. 8, i.e., $\ell = 10a$ and $\psi = 35^\circ$, we obtain $\xi = \zeta_{\perp} / \zeta_{\parallel} = 4 \ln(4q/a) / [2 \ln(4q/a) + 1] \approx 1.37$, which is close to our fitted value $\xi = 1.55$. Since Lighthill's theory does not consider any elasticity of the helical filament or end effects of a finite-size helix (which are all present in our simulations), we suppose the agreement is satisfactory. Although ξ has in fact a weak ψ dependence through the implicit dependence of q on ψ , we ignore this unimportant correction and hereafter use Eq. (25), as is well justified by the good agreement with our numerical data in Fig. 8.

The viscous power dissipation due to the translational motion is calculated according to $P_{dis} = \int_0^L \mathbf{f}(s) \cdot \mathbf{u}(s) ds$, which gives

$$P_{dis} = \frac{\xi}{1 + (\xi - 1)\sin^2 \psi} \zeta_{\parallel} R^2 \omega^2 L, \quad (27)$$

where Eq. (25) has been used. In the free-draining limit, i.e., $\xi = 1$ and $\zeta_{\parallel} = \zeta$, we obtain $P_{dis} = \zeta R^2 \omega^2 L$.

B. Application to a bistable helix

To apply the above result for a rotating uniform helix to our bistable helix, consider now a filament undergoing a dynamic chirality transformation from one chirality to the other. At an intermediate stage of this process, the filament consists of two helical sections of contour-length L_1 (right-handed) and L_2 (left-handed) with $L = L_1 + L_2$. As we have argued before, speedometer-cable motion should be dominant. As the domain wall moves through the filament with velocity V_0 , the right-handed section rotates clockwise at rate ω_1 , while the left-handed section rotates counterclockwise at ω_2 . The rotations of both helical parts propel the whole body into the same direction which is opposite to that of the domain-wall propagation. This mechanism is responsible for *Spiroplasma* propulsion.

The rotational continuity at the junction point leads to the simple geometric relation [70]

$$\omega_1 + \omega_2 = \frac{4\pi V_0}{\ell}. \quad (28)$$

On the other hand, the torque friction balance between the two sections implies $L_1 \omega_1 \approx L_2 \omega_2$, leading, together with Eq. (28), to

$$\omega_1 \approx \frac{4\pi L_2}{\ell L} V_0 \quad \text{and} \quad \omega_2 \approx \frac{4\pi L_1}{\ell L} V_0. \quad (29)$$

Using our calculation for the propulsion velocity U of a rotating helix, Eq. (25), and defining a friction coefficient $\zeta = 3\pi\eta$ per unit length neglecting logarithmic corrections from long-ranged hydrodynamic interactions, the translational propulsive force generated by each helical segment ($\alpha = 1, 2$) is

$$F_{\alpha} \approx \zeta L_{\alpha} U_{\alpha} \approx \zeta L_{\alpha} S \ell \omega_{\alpha}. \quad (30)$$

The total propulsive force on the filament, F , is a vectorial sum of F_1 and F_2 . Neglecting bending deformations of a filament that violate the geometric relation $\Phi = \pi - 2\psi$, we obtain

$$F = (F_1^2 + F_2^2 - 2F_1 F_2 \cos \Phi)^{1/2}. \quad (31)$$

The swimming velocity $v_{\parallel} \approx |d\mathbf{R}_c/dt|$ may be obtained from the viscous balance $\zeta L v_{\parallel} \approx F$. Choosing section lengths $L_1 = d(t)$ and $L_2 = L - d(t)$, we have

$$v_{\parallel}(t) \approx 8\pi \frac{d(t)}{L} \left(1 - \frac{d(t)}{L}\right) S \cos \psi V_0. \quad (32)$$

Inserting the explicit expression of $d(t)$, Eq. (8), and taking the average over one cycle, we obtain

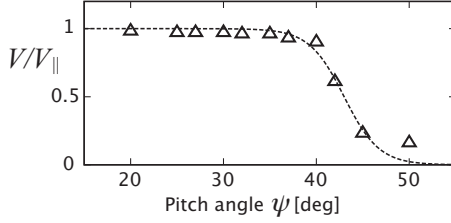


FIG. 9. The ratio of the net velocity to the tangential velocity, V/V_{\parallel} , plotted as a function of pitch angle ψ for a filament with $N=61$, $\bar{A}=10^3$, and $\bar{V}_0=4.0$ (temperature is set to zero). The dotted line is the empirical fitting function, Eq. (36), given in the main text.

$$V_{\parallel} = \frac{1}{T_0} \int_0^{T_0} v_c(t) dt = 8\pi J \left(\frac{\bar{D}}{L} \right) S \cos \psi V_0, \quad (33)$$

where

$$J(x) = \frac{x}{1+x} \left(1 - x + \frac{x^2}{3} \right), \quad (34)$$

and D is replaced by \bar{D} neglecting its small fluctuations. The mean velocity V is given by

$$V = \mu V_{\parallel}, \quad (35)$$

where μ is the geometric factor that accounts for the winding path of the center of mass, compare Fig. 4. The behavior of $\mu = \mu(\psi)$ as function of pitch angle ψ is extracted numerically from the simulation data and is shown in Fig. 9. Although a precise analytical form of $\mu(\psi)$ seems difficult to find, the data fit quite well to the empirical functional form

$$\mu(\psi) = \frac{1}{1 + e^{\lambda(\psi - \psi_0)}}, \quad (36)$$

where the best fit to the data is obtained for $\psi_0 = 43.0^\circ$ and $\lambda = 0.53$. The total power dissipation for this bistable helix is the sum of the translational and rotational or spinning dissipations; see the definition of P_{dis} , Eq. (19). The power dissipation due to translational motion is from Eq. (27) given by

$$P_{dis}^T = \frac{\xi}{1 + (\xi - 1) \sin^2 \psi} \zeta_{\parallel} R^2 (\omega_1^2 L_1 + \omega_2^2 L_2). \quad (37)$$

Inserting Eq. (29), setting $L_1 = d(t)$ and $L_2 = L - d(t)$, and taking again the time average over one cycle, we arrive at the average power dissipation

$$P_{dis}^T = 4J \left(\frac{\bar{D}}{L} \right) \frac{\xi \sin^2 \psi}{1 + (\xi - 1) \sin^2 \psi} \zeta_{\parallel} V_0^2 L, \quad (38)$$

where $2\pi R/\ell = \sin \psi$ has been used. The filament also rotates about its own axis, i.e., it undergoes axial spinning. This axial-spinning velocity, ω , is also supposed to be of order of ω_1 and ω_2 . The power dissipation associated with this mode is thus $P_{dis}^S \approx \pi \eta a^2 \omega^2 L$. Using $\omega \sim \omega_2 = (4\pi/\ell)(d/L)V_0$, and taking the time average over one cycle, we obtain

$$P_{dis}^S = \pi \eta \left(\frac{4\pi a}{\ell} \right)^2 J_s \left(\frac{\bar{D}}{L} \right) V_0^2 L, \quad (39)$$

where

$$J_s(x) = \frac{x^2}{1+x} \left(1 - \frac{x}{3} \right). \quad (40)$$

The total power dissipation is then obtained as

$$P_{dis} = 4\pi \eta V_0^2 L \left[\frac{3 \sin^2 \psi}{1 + (\xi - 1) \sin^2 \psi} J \left(\frac{\bar{D}}{L} \right) + \frac{4\pi^2 a^2}{\ell^2} J_s \left(\frac{\bar{D}}{L} \right) \right], \quad (41)$$

where we have assumed $\xi \zeta_{\parallel} = \zeta_{\perp} \approx 3\pi \eta$ in Eq. (37). The power-conversion efficiency β has been defined as the ratio of the power expended to move a corresponding straight filament of length $L = aN$ at net velocity V [given in Eq. (20)] to the total dissipated power P_{dis} , Eq. (41). The final result is

$$\beta = \frac{(V/V_0)^2}{2 \left[\ln \left(\frac{4L}{a} \right) - 3/2 \right]} \left[\frac{3 \sin^2 \psi}{1 + (\xi - 1) \sin^2 \psi} J \left(\frac{\bar{D}}{L} \right) + \frac{4\pi^2 a^2}{\ell^2} J_s \left(\frac{\bar{D}}{L} \right) \right]^{-1}, \quad (42)$$

where Eqs. (33)–(36) have to be inserted to obtain β as an explicit function of pitch angle ψ .

C. Comparison to numerical data

We show in Fig. 10 the numerically determined rescaled mean velocity V/V_0 , the rescaled tangential velocity V_{\parallel}/V_0 , and the efficiency β (and the total dissipation \tilde{P}_{dis} in the inset) as a function of the pitch angle ψ for $N=61$, $\bar{D}=30a$, and $\bar{V}_0=4.0$. The broken lines in each panel are the corresponding analytic predictions, Eq. (33), (41), and (42), in very nice agreement with our numerical results. To obtain satisfactory agreement both for the velocity and the efficiency data simultaneously, we have taken $\xi=1.67$. Remarkably, both numerical and analytical results show that the swimming velocity and the efficiency take their maximal values at around $\psi \approx 32-37^\circ$, which indeed is very close to the pitch angle for *Spiroplasma melliferium* $\psi \approx 35^\circ$ reported in recent experiments [57]. The bacterium's helical shape is thus optimized for maximal speed and efficiency within the kink-pair propagation mode. A histogram of the domain size distribution is shown in Fig. 10, which was monitored throughout the simulations from which the numerical data shown in (a) and (b) were collected. The distribution is well described by a Gaussian with mean $\bar{D}=30a$ and dispersion $\Delta_{2D}=4a^2$, which are the input parameters.

Real bacteria exhibit significant size variation. In Fig. 11, the rescaled tangential and mean velocities are plotted as a function of the total contour length L divided by the average domain size \bar{D} . Our numerical data show that the tangential swimming speed does not change significantly within the

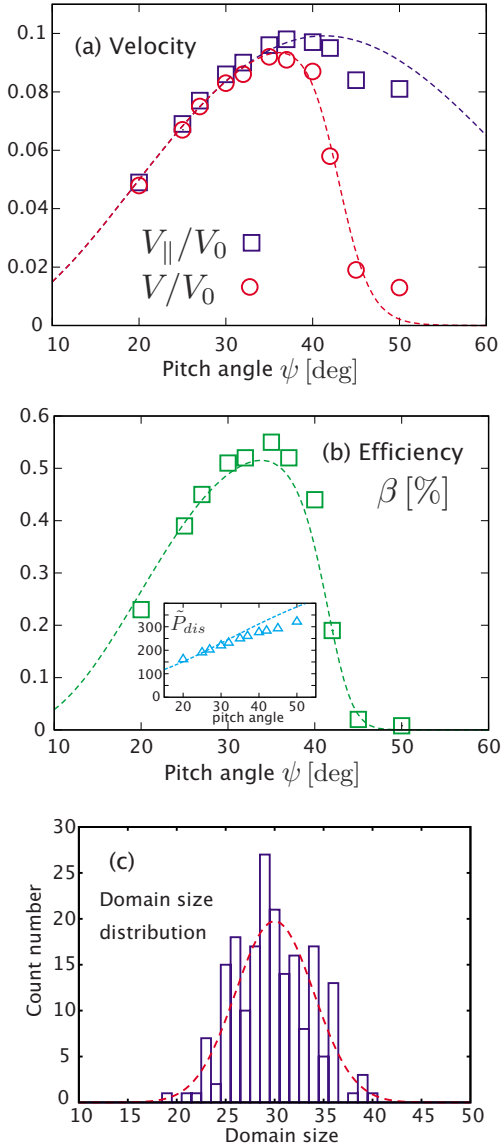


FIG. 10. (Color online) (a) Rescaled tangential velocity, V_{\parallel}/V_0 , (open squares) and mean velocity, V/V_0 , (open circles), obtained from the numerical simulations. The broken lines, red and blue, are respectively the theoretical curves, Eq. (33) and $V = \mu(\psi)V_{\parallel}$. (b) Numerical data for the efficiency β (open squares) as a function of pitch angle ψ for $N=61$, $\tilde{A}=10^3$, and $\tilde{V}_0=4.0$. Broken line is the corresponding analytic theory, Eq. (42). The inset shows the numerical data of the rescaled total power dissipation, \tilde{P}_{dis} , as a function of pitch angle ψ . The broken line is a plot of Eq. (41). (c) The histogram of the domain size distribution throughout the simulations from which the numerical data shown in (a) and (b) were collected. The broken line is a Gaussian with mean $\bar{D}=30a$ and dispersion $\Delta_{D^4}=4a^4$ as prescribed. All data were obtained in zero-temperature simulations.

length ratio studied, i.e., $1 < L/\bar{D} < 5$, consistent with the corresponding analytic prediction, Eq. (33), shown as a broken line in Fig. 11. The theoretical prediction for the mean velocity, $V = \mu V_{\parallel}$, is not shown because it differs only by a small amount from that of V_{\parallel} as $\mu(\psi) \approx 1$ for $\psi = 35^\circ$. For smaller L/\bar{D} , the directional change of the cell body becomes

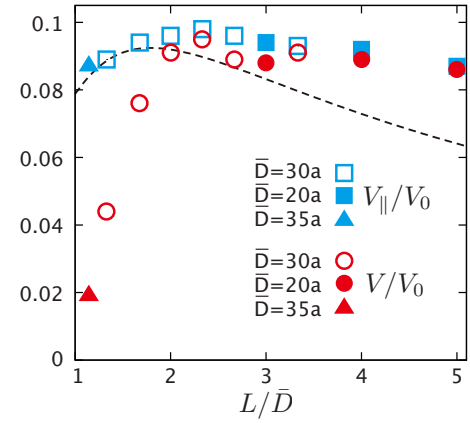


FIG. 11. (Color online) Rescaled tangential velocity, V_{\parallel}/V_0 , (blue square symbols) and mean velocity, V/V_0 , (red circle symbols), plotted as a function of rescaled cell length L/\bar{D} for pitch angle $\psi=35^\circ$, $\tilde{A}=10^3$, and $\tilde{V}_0=4.0$. Data were obtained in zero-temperature simulations. The broken line is the corresponding analytic theory for V_{\parallel}/V_0 , Eq. (33), for a friction ratio $\xi = \zeta_{\perp} / \zeta_{\parallel} = 1.67$.

evident, which makes its “net” velocity, V , significantly smaller. Interestingly, the velocities exhibit a maximum at $L/\bar{D} \sim 2-3$, which in fact is a typical ratio seen in the experiments [51,52,57]. Figure 11 also suggests that data from different combinations of (\bar{D}, L) scale nicely on this plot, showing that the cell length L only determines the swimming speed via the ratio L/\bar{D} , in agreement with our theoretical analysis. The unique kink-pair propagation mode thus provides a rather stable scenario for propulsion for *Spiroplasma* cells of different body lengths. The above numerical results were obtained by fixing the pitch angle at the specific value $\psi = 35^\circ$. Inspection of our analytic expression for the swimming speed in Eq. (33) shows that factorization into a part depending on the pitch angle ψ and a part depending on the length ratio L/\bar{D} is possible, meaning that the optimal parameter set is obtained by separately minimizing with respect to ψ and L/\bar{D} . This is in line with a recent numerical analysis, where a full two parameter optimization over both length ratio, L/\bar{D} , and pitch angle, ψ , has been explored [81]. The optimal combination was found to be $L/\bar{D}=3$ and $\psi=35.5^\circ$ [81]. Considering that the other parameters are slightly different from ours, the agreement with our numerical and analytic results in Figs. 10(a) and 11 is acceptable.

V. EFFECTS OF THERMAL FLUCTUATIONS

A. Biased Brownian motions

So far, thermal Brownian noise was neglected in order to focus on the biomechanical properties of *Spiroplasma* motility. In this section, we include random thermal noise into our Langevin equations and examine the stochastic mean-square displacement of the center of mass of our active filament. The time evolution of the center-of-mass position, $\mathbf{R}_c(t)$, may be understood as a biased Brownian motion whose drifting direction changes due to orientational Brownian motion. For

the center-of-mass motion we suggest the reduced simple Langevin equation

$$\zeta_c \frac{d\mathbf{R}_c}{dt} = \zeta_c V_{\parallel} \hat{\mathbf{n}}(t) + \boldsymbol{\xi}_c(t), \quad (43)$$

where ζ_c is an effective friction constant (which is assumed to be angle averaged since the cell body is rod-shaped and thus anisotropic), V_{\parallel} is the tangential velocity along the contour, and $\hat{\mathbf{n}}(t)$ is the local swimming direction that can change due to Brownian effects. The vectorial translational random thermal noise $\boldsymbol{\xi}_c(t)$ satisfies the fluctuation-dissipation relation, on this level of description given by

$$\langle \boldsymbol{\xi}_c(t) \boldsymbol{\xi}_c(t') \rangle = 2\zeta_c k_B T \mathbf{1} \delta(t-t'). \quad (44)$$

The rotational diffusion equation for a slender, rigid rod of length L and diameter a gives the orientational correlation

$$\langle \hat{\mathbf{n}}(t) \cdot \hat{\mathbf{n}}(0) \rangle = e^{-t/\tau_r}, \quad (45)$$

where the rotational correlation time τ_r is expressed as $\tau_r = 1/(2D_r)$ using the rotational diffusion coefficient given by [80]

$$D_r \approx \frac{3k_B T \ln(L/2R)}{\pi \eta L^3}. \quad (46)$$

Solving Eq. (43) gives the mean-square displacement

$$\langle [\mathbf{R}_c(t) - \mathbf{R}_c(0)]^2 \rangle = 6D_T t + 2V_{\parallel}^2 \tau_r^2 f(t/\tau_r), \quad (47)$$

where $f(x) = e^{-x} + x - 1$ and the translational diffusion coefficient, D_T , has been introduced as

$$D_T = \frac{k_B T}{\zeta_c} \approx \frac{D_{\parallel} + 2D_{\perp}}{3} = \frac{k_B T \ln(L/a)}{3\pi \eta L}. \quad (48)$$

Here D_{\parallel} and D_{\perp} characterize the diffusion parallel and perpendicular to the rod axis and to leading order are given by

$$D_{\parallel} \approx \frac{k_B T \ln(L/a)}{2\pi \eta L}, \quad D_{\perp} \approx \frac{k_B T \ln(L/a)}{4\pi \eta L}. \quad (49)$$

To apply these formulas to our problem, we regard our helical filament as a rod of effective length $(aN)\cos\psi$ and diameter $2R$ [R is the radius of the helix: see Eq. (4)]. Using rescaled variables for the finite-temperature case, the diffusion constant and the rotational correlation time are given, respectively, by $\tilde{D}_T^{(T)} = \ln(L \cos\psi/2R)/(L/a)\cos\psi$ and $\tilde{\tau}_r^{(T)} = (L/a)^3 \cos^3\psi / \ln(L \cos\psi/2R)$. Plugging these expressions, together with $V_{\parallel} \approx 0.096V_0$ obtained from zero-temperature simulations, into Eq. (47), we obtain an analytic formula for the center-of-mass mean square displacement of a self-propelling helix. It is compared to the numerical data in Fig. 12, in good agreement without any adjustable parameters. The simple model presented in Eqs. (43)–(48) captures well the propulsion of the helix in the presence of thermal effects. In fact, the orientational correlation time in Fig. 12 is $\tilde{\tau}_r^{(T)} \approx 2000$, which well exceeds the total simulation time, $\tilde{T}_0^{(T)} = 800$ (corresponding to 4×10^7 time steps in the simulation). For $t/\tau_r \ll 1$, since $f(x) \sim x^2/2$, we have from Eq. (47) $\langle [\mathbf{R}_c(t) - \mathbf{R}_c(0)]^2 \rangle \approx 6D_T t + V_{\parallel}^2 t^2$. Thus, for $t < V_{\parallel}^2/(6D_T)$, thermal diffusion dominates and we have $\sim 6D_T t$, and for

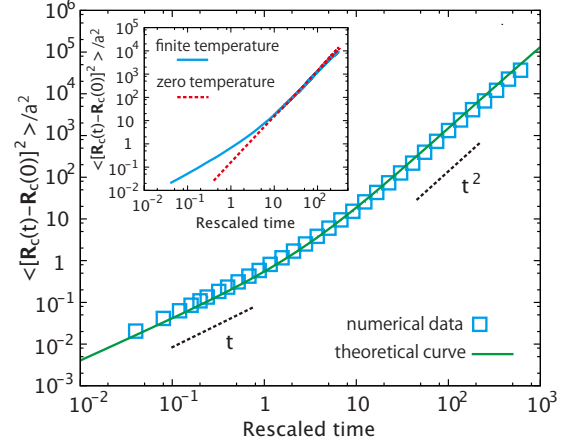


FIG. 12. (Color online) Rescaled mean-square displacement of the filament center-of-mass position, $\langle [\mathbf{R}_c(t) - \mathbf{R}_c(0)]^2 \rangle / a^2$, obtained in finite-temperature simulation for filament size $N=61$, pitch angle $\psi=35^\circ$, and (rescaled) domain-wall speed $\tilde{V}_0^{(T)}=4.0$. The green line is the theoretical prediction, Eq. (47). The inset compares the numerical data for the finite-temperature and zero-temperature cases. We note that the diffusive long-time limit is not reached in the simulations.

$V_{\parallel}^2/(6D_T) \ll t \ll \tau_r$, the active swimming motion (drifting) dominates and we have $V_{\parallel}^2 t^2$, as clearly seen in Fig. 12. The inset of Fig. 12 compares the numerical data in the presence (blue) and in the absence (red) of thermal noise, which clearly shows that the diffusive behavior dominates at short times while at longer times it seems less important. Equation (47) also predicts the simple diffusive behavior $\langle [\mathbf{R}_c(t) - \mathbf{R}_c(0)]^2 \rangle \sim 6D^* t$ for even longer time regime, $t \gg \tau_r$, with the modified translational diffusion coefficient $D^* = D_T + 2V_{\parallel}/\tau_r$. The physical meaning of this is clear; the drift due to the orientational Brownian motion translates into a random translational Brownian motion with an appropriately defined diffusion constant. This long time regime is not attained in Fig. 12, but we have confirmed this second crossover to the normal diffusive behavior with the effective diffusion constant D^* by performing a simulation for a short polymer of $N=41$ monomers for up to 10^8 steps (data not shown).

B. Effects of cell stiffness on the propulsion

As the actual bending rigidity of *Spiroplasma* cells is experimentally not known, it is important to study how the propulsive behavior depends on the helix bending modulus, A . In Fig. 13, the mean-square displacement of the center-of-mass position, \mathbf{R}_c , is plotted for different values of A , i.e., $L_p/a = A/(k_B T a) = 50 - 10^3$, with the twist-bend rigidity ratio $C/A=1$ unchanged. Here we have used a filament of size $N=51$ and pitch angle $\psi=35^\circ$ and used a kink velocity $\tilde{V}_0^{(T)}=4.0$. As the filament becomes softer, it flexes more frequently and significantly due to random thermal fluctuations and the kinking stroke is less efficiently converted to a directional swimming motion, which leads to a reduced propulsion velocity V_{\parallel} . At $L_p=50a$, or $L_p/L=1$, the swimming regime given by $V_{\parallel}^2 t^2$ at long time disappears, and only the

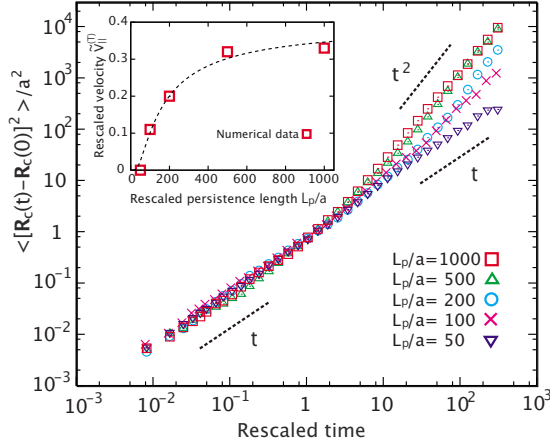


FIG. 13. (Color online) Rescaled mean-square displacement of the filament center-of-mass position, $\langle [\mathbf{R}_c(t) - \mathbf{R}_c(0)]^2 \rangle / a^2$, for different filament stiffness, L_p/a , (with $C/A=1$). Filament length $L=51a$, pitch angle $\psi=35^\circ$, and (rescaled) domain-wall speed $\tilde{V}_0^{(T)}=4.0$ are used in these finite-temperature simulations. The inset shows the rescaled tangential propulsion velocity, $\tilde{V}_\parallel^{(T)}$, as a function of the rescaled persistence length, L_p/a , and a comparison with the heuristic fitting expression Eq. (50), broken line.

normal diffusive behavior proportional to t is observed; see Fig. 13. Except this extreme case, the numerical data for different L_p/a are reasonably fitted by Eq. (47), from which we obtain the effective propulsion velocity V_\parallel as a function of L_p/a . The rescaled velocity $\tilde{V}_\parallel^{(T)}$ is shown in the inset of Fig. 13, where we set $V_\parallel=0$ for $L_p/L=1$. Interestingly, we find that the data can be well described by the functional form

$$V_\parallel = V_\infty e^{-L^*/L_p}, \quad (50)$$

with the velocity in the infinitely-stiff limit denoted by $\tilde{V}_\infty=0.4$, and a crossover length scale, $L^*/a=136$, shown in the inset of Fig. 13. We conclude that a softer cell exhibits decreased swimming speed, but that a drastic speed reduction only sets in when the persistence length becomes smaller than a crossover length on the order of $L^*/a=136$. For a realistic diameter on the order of 100 nm, this amounts to a persistence length of about 10 μm which is not an unrealistic value for biofilaments.

VI. VISCOSITY EFFECTS ON THE MOTILITY

Fluid viscosity has significant consequences on bacterial motility. For externally flagellated bacteria, increase in the swimming speed is observed only for a slightly more viscous medium than buffer; a further increase in viscosity typically reduces the motility [63,65]. On the other hand, helical-shaped headless bacteria such as *Leptospiras* or *Spiroplasma* swim faster in media with higher viscosity, within given limits, specifically in meshlike structure formed by polymers that give rise to conditions similar to their native environments such as phloem vessels, nectaries, and insect lymph systems [52,57,64]. Interplay between a cell-body deforma-

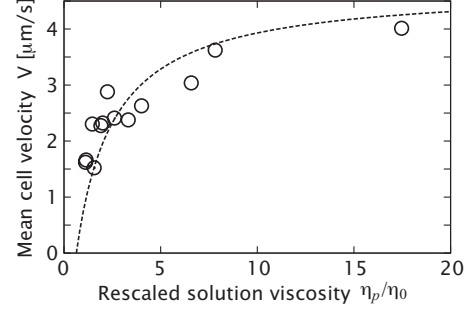


FIG. 14. Mean cell swimming velocity, V , as a function of the solution viscosity η_p , scaled by the water viscosity $\eta_0=1$ cP, η_p/η_0 . The experimental data (open circle) are taken from Gilad *et al.* [52]. The dashed line is the plot of Eq. (52) for pitch angle $\psi=35^\circ$. The best fit to the experimental data is obtained for $V_0 \approx 9.1$ $\mu\text{m/s}$.

tion and the viscoelastic response of the surrounding medium is a difficult task to study, which leaves the problem up to date poorly understood. A fundamental calculation would be highly involved; a simplified approach suggested in Refs. [38,62] in fact provides insight into the influence of viscoelasticity on helical-shaped bacterial motility.

Long linear polymers in solution above the overlap concentration form a loose, transient gel-like structure [80]. When a slender rigid rod, whose length is much larger than the typical mesh size of the polymer network, is immersed in the solution, the network mainly restricts motion normal to the rod axis, while the tangential motion is unhindered. This anisotropic confinement is most easily taken into account by allowing the hydrodynamic friction coefficient ratio, $\xi = \xi_\perp / \xi_\parallel$, to depend on the polymer viscosity (and thus to deviate from $\xi=2$, even in the slender-body limit.). The simplest way is to replace ξ by

$$\xi_p = \frac{\eta_p}{\eta_0} \xi, \quad (51)$$

where the viscosity of the polymer solution η_p is determined via measuring the sedimenting speed of, say, a latex particle of radius $a \sim 10$ μm as done in Ref. [62]. Note that Eq. (51) recovers the purely viscous case for $\eta_p=\eta_0$, where ξ_p depends only on the geometry of the helical filament and reaches $\xi_p=\xi=2$ in the slender-rod limit. Replacing ξ by ξ_p in Eq. (25), we obtain the swimming velocity V as a function of the polymer viscosity η_p :

$$V = 8\pi V_0 J \left(\frac{\bar{D}}{L} \right) \mu(\psi) \cos \psi S_p(\xi \eta_p / \eta_0), \quad (52)$$

where the function S_p has the same form as S , but now is a function of η_p/η_0 and is given by

$$S_p(z) = \frac{(z-1) \sin^2 \psi \cos \psi}{2\pi [1 + (z-1) \sin^2 \psi]}. \quad (53)$$

Equation (52) is compared in Fig. 14 with the experimental data from Ref. [52], showing good agreement. Here, the kink propagation speed V_0 is assumed independent of the solution

viscosity (as confirmed experimentally [52,57]) and is treated as the only fitting parameter yielding $V_0 \approx 9.1 \mu\text{m}/\text{sec}$. In the high viscosity limit, i.e., $\xi_p \rightarrow \infty$, the ratio of the swimming velocity and the domain-wall velocity projected along the helical axis, $V_0 \cos \psi$, becomes

$$V/(V_0 \cos \psi) = 4J \left(\frac{\bar{D}}{L} \right) \mu(\psi) \cos \psi, \quad (54)$$

which, for $\psi=35^\circ$, is about 0.6. In the experiment [57], this value was reported to reach around 0.5 in the media of 0.5% methylcellulose added, and thus consistent with Eq. (54).

Several authors have studied theoretically the effects of viscoelasticity of a surrounding fluid on propulsion with periodically actuated flexible filaments or sheets [82–84]. They were mainly interested in understanding how inertial reactions due to elasticity of the fluid, which are absent in purely viscous fluids, can change the dynamics of beating patterns of flexible objects. On the other hand, our argument, as well as the one first proposed by Magariyama and Kudo [66], is focused more on spatial effects, i.e., effects of a transient confinement due to the formation of a polymer network. Comparison with a generalized theory for the swimming speed of flagellated bacteria in polymeric meshworks shows that the presence of a finite-sized bacterial head gives rise to a maximal swimming speed at a finite solution viscosity (see Appendix A for details). In contrast, as shown in this section, in the absence of a head, as appropriate for *Leptospiras* and *Spiroplasma*, the swimming speed monotonically increases with increasing viscosity.

We add an important remark. Previous studies suggested that *Spiroplasma* could swim in ficoll solutions as fast as in methylcellulose solutions of the same viscosity [52,58]. In contrast, *Leptospiras* is known to swim slower in ficoll solutions. As ficoll solutions supposedly are simple Newtonian fluids, our simplistic argument may not explain the difference observed between *Spiroplasma* and *Leptospiras*. To our knowledge, the only quantitative data on *Spiroplasma* motion in ficoll solutions are published in Ref. [52] and show a slight increase in swimming speed for solutions of two different ficoll concentrations. Reference [58] refers to viscotactic behavior of *Spiroplasma* in ficoll solutions but does not report quantitative data. Experimental uncertainty and lack of sufficient data for *Spiroplasma* motility in ficoll solutions leave the physical picture of the viscosity dependence of *Spiroplasma* motility unclear and additional different physical mechanisms not treated by us could be present as well. More quantitative experimental data of *Spiroplasma* swimming in different polymeric solutions would be highly desirable in order to promote our understanding of this issue. Still, we see our theory as a simple explanation for the experimental fact that the swimming speed of helical-shaped bacteria (such as *Spiroplasma* and *Spirochete* like *Leptospiras*) in methylcellulose solution increases, while the speed of flagellated bacteria decreases for very large viscosity (as we show in Appendix A).

VII. CONCLUSION

In this paper, we have presented analytical and numerical studies on a self-propelling bistable helix as a model system

for *Spiroplasma* bacterial motility. We have constructed an elastic helical rod model that consists of unidirectionally moving domain walls between sections of left- and right-handed helicity. Hydrodynamic simulations revealed the following properties: (i) as a kink pair travels down along the filament the cell itself swims in a direction opposite to the kink propagation, (ii) the linear swimming velocity is proportional to the kink velocity with a proportionality constant in fair agreement with experiments [52,57], (iii) the center-of-mass motion follows a helical trajectory with a pitch close to the pitch of the cell body, (iv) the optimal hydrodynamic propulsion efficiency is obtained at a cell-body pitch angle of $\psi \approx 35^\circ$, very close to the actual pitch of *Spiroplasma*, and (v) the fastest swimming speed for $\psi=35^\circ$ is obtained at domain-size-to-body-length ratio $L/\bar{D} \approx 2-3$, similar to the actual length ratio observed in cells. We also considered the effects of cell-body flexibility, which reduces the swimming speed as the bending persistence length becomes smaller. Analytic arguments based on the slender-body hydrodynamics approximation provide physical interpretations of the propulsion mechanism in quantitative agreement with the numerical findings (and experimental observations). Enhanced motility of *Spiroplasma* in viscoelastic materials has been considered within a semiquantitative analytic approach which takes into account the effects of anisotropic friction due to the presence of a gel-like polymer network in the surrounding fluid and shows a good agreement with experimental data [52]. Making use of the unique swimming mechanism of a *Spiroplasma* bacterium to create an artificial micromachine working efficiently at low Reynolds number would be an intriguing and challenging subject in the development of nano-to-micro technology of soft materials. The results, as well as the numerical and analytical techniques, presented in this study are also applicable to many other interesting problems such as propulsion with flagellarlike helical filaments [85], dynamics of polymorphic transformations in bacterial helical flagellar filaments [69,86–88], and propulsion and shape transitions of synthetic organic materials forming bistable helices [89].

ACKNOWLEDGMENTS

We thank J. W. Shaevitz for valuable discussions. Financial support from the German Science Foundation (DFG Grants No. SPP1164 and No. SFB 486), the German Excellence Initiative via the Nanosystems Initiative Munich (NIM), and the Ministry of Education, Culture, Sports, Science, and Technology (MEXT) of Japan (Grant in Aid, Grant No. 20740241) is acknowledged. The numerical calculations were carried out on Altix3700 BX2 at YITP, Kyoto University.

APPENDIX A: SWIMMING OF EXTERNALLY FLAGELLATED BACTERIA

In this appendix, we present a generalized treatment for the rotational and translational mobilities of a rigid helix in a Stokesian fluid based on the slender-body hydrodynamic approximation. The treatment described here also includes the

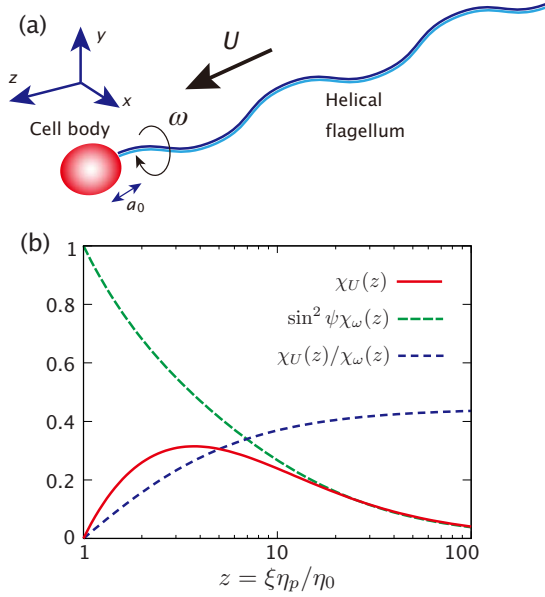


FIG. 15. (Color online) (a) Cartoon of a swimming single-flagellated bacterium with a cell body of radius a_0 and a flagellum of contour length L . (b) Plots of the functions $\chi_U(z)$, $\chi_\omega(z)\sin^2\psi$, and $\chi_U(z)/\chi_\omega(z)$, where $z = \xi\eta_p/\eta_0$, for $\psi = 40^\circ$ and $\nu = 0.3$. η_p is the viscosity of the polymer solution, η_0 is the viscosity of the solvent in the absence of polymers, and ξ is the friction anisotropy for a simple viscous fluid.

swimming of externally flagellated bacteria for arbitrary viscosity ratio η_p/η_0 based on the idea described in Refs. [62,66]. We consider a single polar flagellated bacterium such as *Pseudomonas aeruginosa*; extensions of our result to multiflagellated bacteria such as *E. Coli* are straightforward. We model a bacterial head (cell part) as a sphere of radius a_0 and take its center position at time t as $\mathbf{r}_c = (0, 0, Ut)$, where U is the yet undetermined propulsion velocity. Assuming the flagellar filament as a rigid helix oriented along the helical axis \mathbf{z} , the helix centerline position is given by

$$\mathbf{r}(s, t) = \begin{bmatrix} R \cos(ks + \omega t) \\ R \sin(ks + \omega t) \\ a_0 + bs + Ut \end{bmatrix}, \quad (\text{A1})$$

where $k = 2\pi/\ell = \sin\psi/R$ and $b = \cos\psi$ with ψ being the pitch angle of the flagellar helix; see Fig. 15(a). According to slender-body theory, the force per length, \mathbf{f} , acting on the helix, is

$$\mathbf{f}(s) = \zeta_\perp[\mathbf{u} - (\mathbf{t} \cdot \mathbf{u})\mathbf{t}] + \zeta_\parallel(\mathbf{t} \cdot \mathbf{u})\mathbf{t}, \quad (\text{A2})$$

where $\mathbf{t} = \partial\mathbf{r}/\partial s$ is the local tangent, $\mathbf{u} = \partial\mathbf{r}/\partial t$ is the velocity, and ζ_\perp and ζ_\parallel are the perpendicular and parallel friction coefficients of a cylinder [56,61,80]. Total force acting on the spherical cell body may be given by $\approx 6\pi\eta_p a_0 U$. Let $\mathbf{M} = M\hat{\mathbf{z}}$ be a torque generation by the motor and ω_0 a rotational velocity of the cell body about the helix axis. Since the total force and the torque on the translationally unconstrained helix is zero, the force and torque balance equations read

$$6\pi\eta_p a_0 \hat{\mathbf{z}} + \int_0^L \mathbf{f}(s) ds = \mathbf{0}, \quad (\text{A3})$$

$$M\hat{\mathbf{z}} + \int_0^L \mathbf{f}(s) \times \mathbf{r}_\perp(s) ds = \mathbf{0}, \quad (\text{A4})$$

$$-M + 8\pi\eta_0 a_0^3 \omega_0 = 0, \quad (\text{A5})$$

where $\mathbf{r}_\perp(s) = [R \cos(ks + \omega t), R \sin(ks + \omega t), 0]$. Inserting Eq. (21) and considering the z component of Eqs. (A3) and (A4), we obtain

$$[\zeta_\perp + (\zeta_\parallel - \zeta_\perp)b^2 + 6\pi\eta_p a_0/L]U + (\zeta_\parallel - \zeta_\perp)(kR^2)b\omega = 0, \quad (\text{A6})$$

$$(\zeta_\parallel - \zeta_\perp)(kR^2)bU + [\zeta_\perp + (\zeta_\parallel - \zeta_\perp)(kR)^2]R^2\omega = \frac{M}{L}. \quad (\text{A7})$$

Solving these equations, we find

$$U = \frac{(\zeta_\perp - \zeta_\parallel)\cos\psi}{\zeta_\perp\zeta_\parallel + 3\pi\eta_p a_0/L[\zeta_\perp + (\zeta_\parallel - \zeta_\perp)\sin^2\psi]} \frac{2\pi M}{\ell L}, \quad (\text{A8})$$

$$\omega = \frac{\zeta_\perp + (\zeta_\parallel - \zeta_\perp)\cos^2\psi + \frac{3\pi\eta_p a_0}{L}}{\sin^2\psi \left[\zeta_\perp\zeta_\parallel + \frac{3\pi\eta_p a_0}{L} \{ \zeta_\perp + (\zeta_\parallel - \zeta_\perp)\sin^2\psi \} \right]} \frac{4\pi^2 M}{\ell^2 L}. \quad (\text{A9})$$

For polymeric solutions, the drag perpendicular to the long axis of the flagellar filament can be much larger than the parallel drag due to (transient) confining effects by a polymeric network. Here, we assume $\zeta_\perp/\zeta_\parallel \approx (\eta_p/\eta_0)\xi$, where η_p and η_0 are, respectively, the viscosity of the polymeric fluid and of water, so that the relation $\zeta_\perp/\zeta_\parallel = \xi$ is recovered in the absence of viscous agents, i.e., $\eta_p = \eta_0$. Equations (A8) and (A9) are expressed in the form

$$U = \chi_U(\xi\eta_p/\eta_0) \frac{2\pi M}{\zeta_\parallel \ell L}, \quad (\text{A10})$$

$$\omega = \chi_\omega(\xi\eta_p/\eta_0) \frac{4\pi^2 M}{\zeta_\parallel \ell^2 L}, \quad (\text{A11})$$

where the characteristic functions are

$$\chi_U(z) = \frac{(z-1)\cos\psi}{z + \nu z[z + (1-z)\sin^2\psi]}, \quad (\text{A12})$$

$$\chi_\omega(z) = \frac{z + (1-z)\cos^2\psi + \nu z}{\sin^2\psi[z + \nu z\{z + (1-z)\sin^2\psi\}]}, \quad (\text{A13})$$

and we have introduced the dimensionless head-size to flagellum-length ratio

$$\nu = \frac{3\pi\eta_0 a_0}{\xi\zeta_{\parallel}L}, \quad (\text{A14})$$

which we assume to be a constant determined by geometry only, since ζ_{\parallel} is expected to scale as η_0 independent of η_p , even in the presence of a polymer network. Schematic plots of $\chi_U(z)$ and $\chi_{\omega}(z)$ are shown in Fig. 15, for $\nu=0.3$. Since within our slender-body argument, the friction coefficient parallel to the long axis of the filament remains unchanged with η_p , i.e., $\zeta_{\parallel} \sim \eta_0$, the swimming velocity of an externally flagellated cell, U , takes its maximum value at a finite viscosity value η_p^* for a constant torque generation by the motor M . Further increase in the polymer solution viscosity leads to a monotonic decrease in the swimming speed. The swimming maximum is attained at

$$z^* = \frac{\eta_p^*}{\eta_0} \xi = 1 + \frac{(1 + \nu^{-1})^{1/2}}{\cos \psi}, \quad (\text{A15})$$

with the maximum value of

$$\chi_U(z^*) = \frac{\cos \psi}{[\nu^{1/2} \cos \psi + (1 + \nu)^{1/2}]^2}, \quad (\text{A16})$$

which is larger for smaller ν (i.e., smaller head size-to-flagellar length ratio a_0/L). For $z \gg z^*$, we find $\chi_U(z) \sim (\nu \cos \psi)^{-1/z}$, suggesting that the drag is dominated by the head cell part for a large enough η_p regime. The existence of the maximum speed agrees with the experimental observation on the swimming speed of single-polar flagellated bacteria, *Pseudomonas aeruginosa* [63].

The above argument is directly applicable to a helical-shaped cell without any head such as *Spiroplasma* and *Spirichetae* by simply setting $a_0=0$, which leads to

$$\chi_U^0(z) = \left(1 - \frac{1}{z}\right) \cos \psi, \quad (\text{A17})$$

$$\chi_{\omega}^0(z) = \frac{1}{\sin^2 \psi} \left[1 + \left(1 - \frac{1}{z}\right) \cos^2 \psi\right]. \quad (\text{A18})$$

By taking the ratio of these two functions, we recover Eq. (53):

$$U = S_p(\xi\eta_p/\eta_0)\ell\omega, \quad (\text{A19})$$

$$S_p(z) = \frac{(z-1)\sin^2 \psi \cos \psi}{2\pi[1 + (z-1)\sin^2 \psi]}. \quad (\text{A20})$$

Note that there is no maximum of the swimming speed as the head size a_0 goes to zero and the swimming speed increases monotonically with viscosity. This is again consistent with the previous experimental results for helical-shaped bacterial cells without any head such as *Leptospira interrogans* [64] and *Spiroplasma* [52,57]. This might give us a clue to understand why helical-shaped headless bacteria are preferentially abundant in highly viscous environments [51].

APPENDIX B: SLENDER-BODY LIMIT IN LIGHTHILL'S THEORY

Equation (25) with $\xi=2$ is obtained by taking the singular limit (i.e., vanishing regularization cutoff) in Lighthill's calculation on a helical distribution of Stokeslets [3,39]. Since the slender-body hydrodynamics approximation is valid up to the first order of $1/\log(a/L)$ [61], it becomes exact in the limit of vanishing a/L . In the Lighthill's theory, the calculated translational and rotational velocity U and ω read

$$\frac{4\pi\eta_0}{h}U = \cos \psi \sin \psi [-\ln \epsilon + A_1(\cos \psi) - 1], \quad (\text{B1})$$

$$\begin{aligned} \frac{4\pi\eta_0}{h}R\omega = & \cos^2 \psi [-\ln \epsilon + A_1(\cos \psi) - 1] \\ & + 2 \sin^2 \psi [-\ln \epsilon + A_2(\cos \psi)] - 1, \end{aligned} \quad (\text{B2})$$

where ψ is again the pitch angle of the helix, η_0 is the viscosity of the surrounding fluid, h is the force per length acting on the filament that is assumed to be a constant but whose magnitude is unspecified, and

$$\epsilon = \sqrt{e}/2(ka) = 0.82(2\pi a/\ell) \quad (\text{B3})$$

is the regularization cutoff length of the singular Stokeslet suggested by Lighthill [3,39]. The characteristic functions appearing in Eqs. (B1) and (B2) are given by

$$A_1(x) = \ln \epsilon + \int_{\epsilon}^{\infty} \frac{\theta \sin \theta d\theta}{[x^2\theta^2 + 2(1-x^2)(1-\cos \theta)]^{3/2}} \quad (\text{B4})$$

and

$$A_2(x) = \ln \epsilon + \int_{\epsilon}^{\infty} \frac{\sin^2 \theta d\theta}{[x^2\theta^2 + 2(1-x^2)(1-\cos \theta)]^{3/2}}. \quad (\text{B5})$$

In the singular limit $\epsilon \approx a/\ell \rightarrow 0$, U and ω both logarithmically diverge. However, since the regularized functions A_1 and A_2 are insensitive to the change in ϵ and remain finite, we find the ratio $U/(\ell\omega)$ in this limit converges to

$$U/(\ell\omega) \rightarrow \frac{\sin^2 \psi \cos \psi}{2\pi(1 + \sin^2 \psi)} \quad \text{for } \epsilon \rightarrow 0, \quad (\text{B6})$$

which coincides with the result in Eq. (25) for $\xi=2$.

APPENDIX C: KINEMATICS

Consider an inextensible filament of, in general, noncircular cross section of typical size a_0 embedded in three-dimensional space. When $L \gg a_0$, where L is the total arclength of the filament, the configuration of the filament may be described as a spatial curve with its centerline parametrized by the arclength s , $0 \leq s \leq L$. A material orthonormal frame (i.e., the generalized Frenet basis) $\{\hat{\mathbf{e}}_1, \hat{\mathbf{e}}_2, \hat{\mathbf{e}}_3\}$ is defined at each point along the centerline of the moving filament, $\mathbf{r}(s, t)$, where $\hat{\mathbf{e}}_3 = \partial \mathbf{r} / \partial s$ points along the tangent and $\hat{\mathbf{e}}_1$ and $\hat{\mathbf{e}}_2$ correspond to the principle axes of the cross section. In this paper, we take a right-handed triad of unit vectors $\{\hat{\mathbf{e}}_{\mu}\}$,

where $\mu=1,2,3$. The kinematics of the filament evolution can be described via evolution equations of the basis $\{\hat{\mathbf{e}}_\mu\}$ with respect to arclength s and time t [90]:

$$\partial_s \hat{\mathbf{e}}_\mu = \sum_{\nu=1}^3 K_{\mu\nu} \cdot \hat{\mathbf{e}}_\nu = - \sum_{\nu=1}^3 \hat{\mathbf{e}}_\nu \cdot K_{\nu\mu}, \quad (\text{C1})$$

$$\partial_t \hat{\mathbf{e}}_\mu = \sum_{\nu=1}^3 W_{\mu\nu} \cdot \hat{\mathbf{e}}_\nu = - \sum_{\nu=1}^3 \hat{\mathbf{e}}_\nu \cdot W_{\nu\mu}, \quad (\text{C2})$$

where $\partial_{s/t}$ denotes the partial derivative with respect to s/t . \mathbf{K} and \mathbf{W} are the antisymmetric 3×3 matrices (thus $\mathbf{K}^t = -\mathbf{K}$ and $\mathbf{W}^t = -\mathbf{W}$) given by

$$\mathbf{K} = \begin{bmatrix} 0 & \Omega_3 & -\Omega_2 \\ -\Omega_3 & 0 & \Omega_1 \\ \Omega_2 & -\Omega_1 & 0 \end{bmatrix} \quad (\text{C3})$$

and

$$\mathbf{W} = \begin{bmatrix} 0 & \omega_3 & -\omega_2 \\ -\omega_3 & 0 & \omega_1 \\ \omega_2 & -\omega_1 & 0 \end{bmatrix}. \quad (\text{C4})$$

Introducing the strain rate vector

$$\boldsymbol{\Omega} = \Omega_1 \hat{\mathbf{e}}_1 + \Omega_2 \hat{\mathbf{e}}_2 + \Omega_3 \hat{\mathbf{e}}_3 \quad (\text{C5})$$

and the angular velocity vector

$$\boldsymbol{\omega} = \omega_1 \hat{\mathbf{e}}_1 + \omega_2 \hat{\mathbf{e}}_2 + \omega_3 \hat{\mathbf{e}}_3, \quad (\text{C6})$$

the kinematic relations (C1) and (C2) can be expressed in more familiar forms:

$$\partial_s \hat{\mathbf{e}}_\mu = \boldsymbol{\Omega} \times \hat{\mathbf{e}}_\mu \quad \text{and} \quad \partial_t \hat{\mathbf{e}}_\mu = \boldsymbol{\omega} \times \hat{\mathbf{e}}_\mu. \quad (\text{C7})$$

The strain rates and angular velocities are obtained from spatial and temporal changes of the basis vectors:

$$\Omega_1 = \hat{\mathbf{e}}_3 \cdot \partial_s \hat{\mathbf{e}}_2 = -\hat{\mathbf{e}}_2 \cdot \partial_s \hat{\mathbf{e}}_3, \quad (\text{C8})$$

$$\Omega_2 = -\hat{\mathbf{e}}_3 \cdot \partial_s \hat{\mathbf{e}}_1 = \hat{\mathbf{e}}_1 \cdot \partial_s \hat{\mathbf{e}}_3, \quad (\text{C9})$$

$$\Omega_3 = \hat{\mathbf{e}}_2 \cdot \partial_s \hat{\mathbf{e}}_1 = -\hat{\mathbf{e}}_1 \cdot \partial_s \hat{\mathbf{e}}_2, \quad (\text{C10})$$

and

$$\omega_1 = \hat{\mathbf{e}}_3 \cdot \partial_t \hat{\mathbf{e}}_2 = -\hat{\mathbf{e}}_2 \cdot \partial_t \hat{\mathbf{e}}_3, \quad (\text{C11})$$

$$\omega_2 = -\hat{\mathbf{e}}_3 \cdot \partial_t \hat{\mathbf{e}}_1 = \hat{\mathbf{e}}_1 \cdot \partial_t \hat{\mathbf{e}}_3, \quad (\text{C12})$$

$$\omega_3 = \hat{\mathbf{e}}_2 \cdot \partial_t \hat{\mathbf{e}}_1 = -\hat{\mathbf{e}}_1 \cdot \partial_t \hat{\mathbf{e}}_2. \quad (\text{C13})$$

Ω_1 and Ω_2 are the bending strain rates with respect to the two principle axes of the cross section and Ω_3 represents the twist density. Likewise, ω_1 and ω_2 are the angular velocities of the tangent around the two principle axes and ω_3 is the angular velocity about the tangent. Specifically, the rotation angle about the tangent $\phi(s, t)$ can be introduced through the variational relation

$$\delta\phi = \hat{\mathbf{e}}_2 \cdot \delta\hat{\mathbf{e}}_1 = -\hat{\mathbf{e}}_1 \cdot \delta\hat{\mathbf{e}}_2, \quad (\text{C14})$$

which, when compared to Eqs. (C10) and (C13), leads to

$$\Omega_3 = \frac{\partial}{\partial s} \phi \quad \text{and} \quad \omega_3 = \frac{\partial}{\partial t} \phi. \quad (\text{C15})$$

Once the basis vectors $\{\hat{\mathbf{e}}_\mu\}$ are known at a given time t , the instantaneous filament shape is reconstructed by

$$\mathbf{r}(s, t) = \mathbf{r}(0, t) + \int_0^s \hat{\mathbf{e}}_3(s', t) ds'. \quad (\text{C16})$$

The filament shape is alternatively described by the original Frenet formulation of space curves in terms of the unit tangent $\hat{\mathbf{t}} = \hat{\mathbf{e}}_3$, normal $\hat{\mathbf{n}} = \partial_s^2 \mathbf{r} / |\partial_s^2 \mathbf{r}|$, and binormal vector $\hat{\mathbf{b}} = \hat{\mathbf{e}}_3 \times \hat{\mathbf{n}}$. They satisfy the Frenet equations [91]

$$\partial_s \hat{\mathbf{t}} = \kappa \hat{\mathbf{n}}, \quad (\text{C17})$$

$$\partial_s \hat{\mathbf{n}} = -\kappa \hat{\mathbf{t}} + \tau \hat{\mathbf{b}}, \quad (\text{C18})$$

$$\partial_s \hat{\mathbf{b}} = -\tau \hat{\mathbf{n}}, \quad (\text{C19})$$

where κ is the curvature related to (Ω_1, Ω_2) via $\kappa = (\Omega_1^2 + \Omega_2^2)^{1/2}$ and τ is the torsion. Transformation from one description to the other is obtained via the rotation by an angle φ about the common tangent $\hat{\mathbf{t}} = \hat{\mathbf{e}}_3$, that is,

$$\hat{\mathbf{e}}_1 + i\hat{\mathbf{e}}_2 = \exp[-i\varphi(s)](\hat{\mathbf{n}} + i\hat{\mathbf{b}}). \quad (\text{C20})$$

Plugging this into Eqs. (C17)–(C19), and comparing with Eq. (C7), we obtain the relation between the strain rate $\boldsymbol{\Omega}$ and the curvature κ and torsion τ as

$$\Omega_1 = \kappa \sin \varphi, \quad (\text{C21})$$

$$\Omega_2 = \kappa \cos \varphi, \quad (\text{C22})$$

$$\Omega_3 = \tau + \frac{d\varphi}{ds}. \quad (\text{C23})$$

For an equilibrium (stress-free) state, twist about the local tangent is absent ($\varphi=0$), the intrinsic torsion τ_0 is therefore equal to Ω_3^0 , leading to

$$\Omega_1^0 = 0, \quad \Omega_2^0 = \kappa_0, \quad \text{and} \quad \Omega_3^0 = \tau_0. \quad (\text{C24})$$

The ground-state shape of a filament is completely specified by the intrinsic curvature κ_0 and torsion τ_0 , which are in general determined by geometrical parameters of a filament equilibrium shape.

APPENDIX D: METHOD OF THE ELASTO-HYDRODYNAMIC SIMULATION

In this appendix, we describe details of our numerical simulation method. The basic idea was first proposed by Allison *et al.* [92] and later significantly improved and refined by Chirico and Langowski [71,72]. The extension and generalization of those methods presented below allow us to

study the nonlinear elasto-hydrodynamics of an elastic filament with an arbitrary ground-state shape and anisotropies and nonuniformities of the elastic moduli.

1. Parametrization

In our Brownian dynamic simulation, the filament is modeled as a chain of $N+1$ connected spheres of diameter a . Each bead is specified by its position \mathbf{r}_i and a body-fixed right-handed frame (expressed as the 3×3 matrix form) [92,71]:

$$\mathbf{E}_i \equiv [\hat{\mathbf{e}}_{1,i}, \hat{\mathbf{e}}_{2,i}, \hat{\mathbf{e}}_{3,i}], \quad (\text{D1})$$

which, in the continuum limit ($a \rightarrow 0$ and $N \rightarrow \infty$), corresponds to the material orthogonal frame $\{\hat{\mathbf{e}}_\nu\}$, ($\nu=1,2,3$) introduced in Appendix C. The unit tangent vector is given by

$$\mathbf{e}_{3,i} = \frac{\mathbf{u}_i}{|\mathbf{u}_i|} = \frac{\mathbf{r}_{i+1} - \mathbf{r}_i}{|\mathbf{r}_{i+1} - \mathbf{r}_i|}, \quad (\text{D2})$$

where $\mathbf{u}_i = \mathbf{r}_{i+1} - \mathbf{r}_i$ is the bond vector connecting the monomer i and $i+1$. A finite-angle Euler transformation matrix, $\mathbf{T}(\alpha_i, \beta_i, \gamma_i)$, transforms \mathbf{E}_i into \mathbf{E}_{i+1} . Once the three Euler angles $\alpha_i, \beta_i, \gamma_i$ are known for $i=1, 2, \dots, N$, the chain configuration is reconstructed from

$$\mathbf{r}_{i+1} = \mathbf{r}_i + a\hat{\mathbf{e}}_{3,i}, \quad (\text{D3})$$

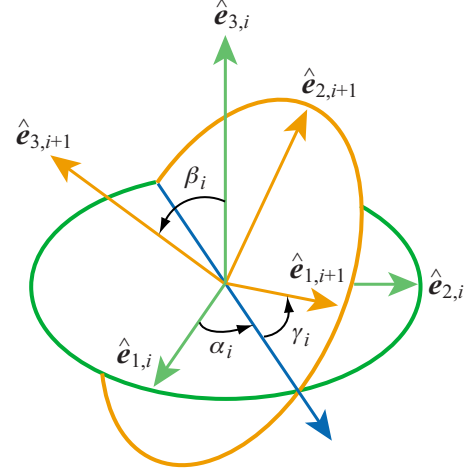


FIG. 16. (Color online) Transformation of the coordinate \mathbf{E}_i to \mathbf{E}_{i+1} parametrized by the Euler angles $(\alpha_i, \beta_i, \gamma_i)$.

$$\mathbf{E}_{i+1} = \mathbf{E}_i \cdot \mathbf{T}(\alpha_i, \beta_i, \gamma_i), \quad (\text{D4})$$

which is the discrete version of Eq. (C16).

There are a few different definitions of the Euler angle transformation in literature. For completeness, we give the explicit form of the matrix that we use in this paper (see also Fig. 16):

$$\mathbf{T}(\alpha, \beta, \gamma) = \begin{bmatrix} \cos \alpha \cos \beta \cos \gamma - \sin \alpha \sin \gamma & -\cos \alpha \cos \beta \sin \gamma - \sin \alpha \cos \gamma & \cos \alpha \sin \beta \\ \sin \alpha \cos \beta \cos \gamma + \cos \alpha \sin \gamma & -\sin \alpha \cos \beta \sin \gamma + \cos \alpha \cos \gamma & \sin \alpha \sin \beta \\ -\sin \beta \cos \gamma & \sin \beta \sin \gamma & \cos \beta \end{bmatrix}. \quad (\text{D5})$$

Specifically, the following relation will be repeatedly used below:

$$\hat{\mathbf{e}}_{\mu,i} \cdot \hat{\mathbf{e}}_{\nu,i+1} = T_{\mu\nu}(\alpha_i, \beta_i, \gamma_i) \equiv (T_i)_{\mu\nu}. \quad (\text{D6})$$

Examining an infinitesimal rotation by matrix (D5), we find the generator matrix of such a rotational transformation, which is the matrix \mathbf{K} in Eq. (C3), giving the strain rates Ω on the discrete points in terms of the Euler angles as [73]

$$\Omega_{1,i} a = -\beta_i \sin \alpha_i, \quad (\text{D7})$$

$$\Omega_{2,i} a = \beta_i \cos \alpha_i, \quad (\text{D8})$$

$$\Omega_{3,i} a = \alpha_i + \gamma_i, \quad (\text{D9})$$

for $i=1, 2, \dots, N$. Noting Eq. (C24) and the intrinsic values of the Euler angles that satisfy the relations $\Omega_1^0 = -\beta_0 \sin \alpha_0 = 0$, $\Omega_2^0 = \beta_0 \cos \alpha_0 = \kappa_0$, and $\Omega_3^0 = \alpha_0 + \gamma_0 = 0$, we conclude that

$$\alpha_0 = 0, \quad \beta_0 = \kappa_0, \quad \text{and} \quad \gamma_0 = \tau_0. \quad (\text{D10})$$

2. Elastic energy

Since the strain rate vector is given at each sphere point according to Eqs. (D7)–(D9), the bending and twisting energy in our bead-spring description is obtained from Eq. (3) in terms of the Euler angles (α, β, γ) . The total elastic energy in the system includes the stretching contribution ensuring the connectivity of spheres:

$$E_{tot} = \sum_{i=1}^{N+1} [E_{str} + E_{bend} + E_{twist}], \quad (\text{D11})$$

where

$$E_{str} = \frac{K}{2a^2} (|\mathbf{r}_{i+1} - \mathbf{r}_i| - a)^2, \quad (\text{D12})$$

$$E_{bend} = \frac{A_1}{2a} (\beta_i \sin \alpha_i)^2 + \frac{A_2}{2a} (\beta_i \cos \alpha_i - \kappa_0)^2, \quad (\text{D13})$$

$$E_{twist} = \frac{C}{2a} (\alpha_i + \gamma_i - \tau_0)^2, \quad (\text{D14})$$

where the bending rigidities A_1 and A_2 can differ. For an isotropic, intrinsically straight rod, i.e., $A_1 = A_2 = A$ and $\kappa_0 = 0$, U_{bend} is reduced to a more familiar form that depends only on β : $E_{bend} = (A/2a)\beta^2$, widely used in previous studies [71,72,92,93].

3. Calculation of force and torque

We proceed to compute the elastic force and torque acting on each monomer from the elastic energy (D11) and write them as functions of \mathbf{r}_i and $\{\hat{\mathbf{e}}_{\mu,i}\}$ only. According to the principle of virtual work, the force \mathbf{F}_i acting on the i th sphere is obtained by varying the position \mathbf{r}_i without rotating any element of the filament about the tangent direction. Likewise, the tangential component of the torque M_i is obtained by virtually rotating the rod along the tangent without moving the filament position [94], meaning

$$\begin{aligned} \delta \sum_{i=1}^{N+1} E_{bend} &= \sum_{i=1}^{N+1} A_1 \Omega_{1,i} \delta \Omega_{1,i} + A_2 (\Omega_{2,i} - \Omega_2^0) \delta \Omega_{2,i} \\ &= - \sum_{i=1}^{N+1} \mathbf{F}_i^b \cdot \delta \mathbf{r}_i - \sum_{i=1}^{N+1} M_i^b \delta \phi_i \end{aligned} \quad (\text{D15})$$

and

$$\begin{aligned} \delta \sum_{i=1}^{N+1} E_{twist} &= \sum_{i=1}^{N+1} C (\Omega_{3,i} - \Omega_3^0) \delta \Omega_{3,i} \\ &= - \sum_{i=1}^{N+1} \mathbf{F}_i^t \cdot \delta \mathbf{r}_i - \sum_{i=1}^{N+1} M_i^t \delta \phi_i. \end{aligned} \quad (\text{D16})$$

The stretching energy is also treated in the same way, which is straightforward. There are two main steps in obtaining the force and torque. First, we need to compute β and $\alpha + \gamma$ from the basis $\{\hat{\mathbf{e}}_{\mu}\}$ to evaluate the strain rate vector $\boldsymbol{\Omega}$ at each monomer point. This is achieved by using the relations [71,92]

$$\cos \beta_i = \hat{\mathbf{e}}_{3,i} \cdot \hat{\mathbf{e}}_{3,i+1}, \quad (\text{D17})$$

$$\cos(\alpha_i + \gamma_i) = \frac{\hat{\mathbf{e}}_{1,i+1} \cdot \hat{\mathbf{e}}_{2,i} + \hat{\mathbf{e}}_{2,i+1} \cdot \hat{\mathbf{e}}_{1,i}}{1 + \cos \beta_i}, \quad (\text{D18})$$

$$\sin(\alpha_i + \gamma_i) = \frac{\hat{\mathbf{e}}_{1,i+1} \cdot \hat{\mathbf{e}}_{2,i} - \hat{\mathbf{e}}_{2,i+1} \cdot \hat{\mathbf{e}}_{1,i}}{1 + \cos \beta_i}, \quad (\text{D19})$$

and inverting the sine and cosine in the range $[-\pi, \pi]$. The validity of this procedure is limited to the range $|\alpha + \gamma| \leq \pi$ and $|\beta| \leq \pi$, which is usually satisfied for reasonably large N and small enough time step in the numerical integration. Once we know the value of $\{\beta_i\}$, we obtain $\Omega_{1,i}$ and $\Omega_{2,i}$ by utilizing Eqs. (D5) and (D6) as

$$\Omega_{1,i} = -\beta_i \frac{(T_i)_{23}}{\sin \beta_i} = -\frac{\beta_i}{\sin \beta_i} (\hat{\mathbf{e}}_{2,i} \cdot \hat{\mathbf{e}}_{3,i+1}), \quad (\text{D20})$$

$$\Omega_{2,i} = \beta_i \frac{(T_i)_{13}}{\sin \beta_i} = \frac{\beta_i}{\sin \beta_i} (\hat{\mathbf{e}}_{1,i} \cdot \hat{\mathbf{e}}_{3,i+1}), \quad (\text{D21})$$

and $\Omega_{3,i} = \alpha_i + \gamma_i$, where $(T_i)_{\mu\nu}$ is the (μ, ν) component of the matrix $\mathbf{T}(\alpha_i, \beta_i, \gamma_i)$.

The second step is to calculate the changes in the strain rate due to the virtual displacements $\delta \mathbf{r}$ and $\delta \phi$. We note the following relations:

$$\delta \Omega_{1,i} = -\delta \beta_i \sin \alpha_i - \beta_i \cos \alpha_i \delta \alpha_i, \quad (\text{D22})$$

$$\delta \Omega_{2,i} = \delta \beta_i \cos \alpha_i - \beta_i \sin \alpha_i \delta \alpha_i, \quad (\text{D23})$$

$$\delta \Omega_{3,i} = \delta(\alpha_i + \gamma_i). \quad (\text{D24})$$

The infinitesimal changes in the Euler angles, $\delta \alpha$, $\delta \beta$, and $\delta(\alpha + \gamma)$, can be written in terms of $\delta \mathbf{r}$ and $\delta \phi$ as

$$\begin{aligned} \delta \alpha_i &= -\delta \phi_i + \frac{1}{2} (\mathbf{A}_i^+ + \mathbf{A}_i^-) (\delta \mathbf{r}_{i+2} - \delta \mathbf{r}_{i+1}) \\ &\quad + \frac{1}{2} (\mathbf{B}_i^+ + \mathbf{B}_i^-) (\delta \mathbf{r}_{i+1} - \delta \mathbf{r}_i), \end{aligned} \quad (\text{D25})$$

$$\delta \beta_i = -\mathbf{C}_i (\delta \mathbf{r}_{i+2} - \delta \mathbf{r}_{i+1}) - \mathbf{D}_i (\delta \mathbf{r}_{i+1} - \delta \mathbf{r}_i), \quad (\text{D26})$$

$$\delta(\alpha_i + \gamma_i) = \delta \phi_{i+1} - \delta \phi_i + \mathbf{A}_i^+ (\delta \mathbf{r}_{i+2} - \delta \mathbf{r}_{i+1}) + \mathbf{B}_i^+ (\delta \mathbf{r}_{i+1} - \delta \mathbf{r}_i), \quad (\text{D27})$$

where

$$\mathbf{A}_i^+ = \frac{(T_i)_{32} \hat{\mathbf{e}}_{1,i+1} - (T_i)_{31} \hat{\mathbf{e}}_{2,i+1}}{u_{i+1} [1 + (T_i)_{33}]}, \quad (\text{D28})$$

$$\mathbf{A}_i^- = \frac{(T_i)_{32} \hat{\mathbf{e}}_{1,i+1} - (T_i)_{31} \hat{\mathbf{e}}_{2,i+1}}{u_{i+1} [1 - (T_i)_{33}]}, \quad (\text{D29})$$

$$\mathbf{B}_i^+ = \frac{-(T_i)_{23} \hat{\mathbf{e}}_{1,i+1} + (T_i)_{13} \hat{\mathbf{e}}_{2,i+1}}{u_i [1 + (T_i)_{33}]}, \quad (\text{D30})$$

$$\mathbf{B}_i^- = \frac{(T_i)_{23} \hat{\mathbf{e}}_{1,i+1} - (T_i)_{13} \hat{\mathbf{e}}_{2,i+1}}{u_i [1 - (T_i)_{33}]}, \quad (\text{D31})$$

$$\mathbf{C}_i = \frac{\hat{\mathbf{e}}_{3,i} - (T_i)_{33} \hat{\mathbf{e}}_{3,i+1}}{u_{i+1} \sin \beta_i}, \quad (\text{D32})$$

$$\mathbf{D}_i = \frac{\hat{\mathbf{e}}_{3,i+1} - (T_i)_{33} \hat{\mathbf{e}}_{3,i}}{u_i \sin \beta_i}. \quad (\text{D33})$$

Again, note that $(T_i)_{\mu\nu}$ is written in terms of only $\{\hat{\mathbf{e}}_{\mu}\}$ via Eq. (D6). Details of the derivation of Eqs. (D25)–(D33) are found in Refs. [71,72]. Putting Eqs. (D25)–(D33) into Eqs. (D22)–(D24), we can write down the virtual changes in the strain rate vectors in terms of only $\{\hat{\mathbf{e}}_{\mu}\}$, $\delta \mathbf{r}$, and $\delta \phi$. Finally, from Eq. (D15), we obtain the bending force

$$\mathbf{F}_i^b = -g_i \mathbf{D}_i - g_{i-1} (\mathbf{C}_{i-1} - \mathbf{D}_{i-1}) + g_{i-2} \mathbf{C}_{i-2} - \frac{1}{2} [h_i (\mathbf{B}_i^+ + \mathbf{B}_i^-) - h_{i-1} (\mathbf{A}_{i-1}^+ - \mathbf{B}_{i-1}^+ + \mathbf{A}_{i-1}^- - \mathbf{B}_{i-1}^-) - h_{i-2} (\mathbf{A}_{i-2}^+ + \mathbf{A}_{i-2}^-)], \quad (\text{D34})$$

and the bending torque

$$M_i^b = -h_i, \quad (\text{D35})$$

where we have defined

$$g_i = \frac{1}{\beta_i} [A_1 \Omega_{1,i} (\Omega_{1,i} - \Omega_1^0) + A_2 \Omega_{2,i} (\Omega_{2,i} - \Omega_2^0)] \quad (\text{D36})$$

and

$$h_i = A_1 \Omega_{2,i} (\Omega_{1,i} - \Omega_1^0) - A_2 \Omega_{1,i} (\Omega_{2,i} - \Omega_2^0). \quad (\text{D37})$$

Similarly, from Eq. (D16), the twisting force and torque are obtained, respectively, as

$$\mathbf{F}_i^t = -C (\Omega_{3,i} - \Omega_3^0) \mathbf{B}_i^+ - C (\Omega_{3,i-1} - \Omega_3^0) (\mathbf{B}_{i-1}^+ - \mathbf{A}_{i-1}^+) + C (\Omega_{3,i-2} - \Omega_3^0) \mathbf{A}_{i-2}^+, \quad (\text{D38})$$

$$M_i^t = C (\Omega_{3,i} - \Omega_{3,i-1}). \quad (\text{D39})$$

4. Boundary conditions

We assume force- and torque-free boundary conditions for both ends of the filament. The natural boundary conditions suggest

$$\mathbf{\Omega}_0 = \mathbf{\Omega}^0, \quad \partial_s \mathbf{\Omega}_0 = \mathbf{0} \quad \text{and} \quad \mathbf{\Omega}_{N+1} = \mathbf{\Omega}^0, \quad (\text{D40})$$

where $\mathbf{\Omega}^0 = (\Omega_1^0, \Omega_2^0, \Omega_3^0)$ denotes the strain rate at an equilibrium or stress-free state. Note that the strain rate at the first monomer, $\mathbf{\Omega}_1$, is not necessarily equal to the equilibrium value $\mathbf{\Omega}^0$. As implied in Eqs. (D17)–(D19), to compute $(\alpha_N, \beta_N, \gamma_N)$ (thus $\mathbf{\Omega}_N$), we need to evaluate $\mathbf{E}_{N+1} = \{\hat{\mathbf{e}}_{N+1, \mu}\}$. This is achieved by using Eq. (D4) and condition (D40):

$$\mathbf{E}_{N+1} = \mathbf{E}_N \cdot \mathbf{T}(\alpha_0, \beta_0, \gamma_0) \quad (\text{D41})$$

for any given \mathbf{E}_N at any time t . On the other hand, the boundary conditions, $\mathbf{\Omega}_0 = \mathbf{\Omega}^0$ and $\partial_s \mathbf{\Omega}_0 = \mathbf{0}$, imply $\mathbf{\Omega}_{-1} = \mathbf{\Omega}_0 = \mathbf{\Omega}^0$. Using this, we can compute the force and torque field at monomer $i=1$ without knowing \mathbf{E}_0 . Taken together, the boundary conditions, Eq. (D40), uniquely provide the forces and torques for any given configuration of the filament (specified by $\mathbf{E}_{i=1,2,\dots,N}$ and $\phi_{i=1,2,\dots,N}$) at any given time t .

-
- [1] G. I. Taylor, Proc. R. Soc. London, Ser. A **209**, 447 (1951).
 [2] S. Childress, *Mechanics of Swimming and Flying* (Cambridge University Press, New York, 1981).
 [3] J. Lighthill, SIAM Rev. **18**, 161 (1976).
 [4] E. M. Purcell, Am. J. Phys. **45**, 3 (1977).
 [5] E. M. Purcell, Proc. Natl. Acad. Sci. U.S.A. **94**, 11307 (1997).
 [6] A. Najafi and R. Golestanian, Phys. Rev. E **69**, 062901 (2004).
 [7] J. E. Avron, O. Gat, and O. Kenneth, Phys. Rev. Lett. **93**, 186001 (2004).
 [8] L. E. Becker, S. A. Koehler, and H. A. Stone, J. Fluid Mech. **490**, 15 (2003).
 [9] D. Tam and A. E. Hosoi, Phys. Rev. Lett. **98**, 068105 (2007).
 [10] O. Raz and J. E. Avron, New J. Phys. **9**, 437 (2007).
 [11] J. Gray and G. J. Hancock, J. Exp. Biol. **32**, 802 (1955).
 [12] K. E. Machin, J. Exp. Biol. **35**, 796 (1958).
 [13] J. J. L. Higdon, J. Fluid Mech. **94**, 331 (1979).
 [14] C. H. Wiggins and R. E. Goldstein, Phys. Rev. Lett. **80**, 3879 (1998).
 [15] C. W. Wolgemuth, T. R. Powers, and R. E. Goldstein, Phys. Rev. Lett. **84**, 1623 (2000).
 [16] S. Camalet and F. Jülicher, New J. Phys. **2**, 24 (2000).
 [17] M. C. Lagomarsino, F. Capuani, and C. P. Lowe, J. Theor. Biol. **224**, 215 (2003).
 [18] M. Reichert and H. Stark, Phys. Rev. E **69**, 031407 (2004).
 [19] H. Wada and R. R. Netz, Europhys. Lett. **75**, 645 (2006).
 [20] H. Flores, E. Lobaton, S. Mendez-Diez, S. Tlupova, and R. Cortez, Bull. Math. Biol. **67**, 137 (2005).
 [21] Y. Gebremichael, G. S. Ayton, and G. A. Voth, Biophys. J. **91**, 3640 (2006).
 [22] M. J. Kim and T. R. Powers, Phys. Rev. E **71**, 021914 (2005).
 [23] M. Manghi, X. Schlagberger, Y.-W. Kim, and R. R. Netz, Soft Matter **2**, 653 (2006).
 [24] J. R. Blake, Math. Methods Appl. Sci. **24**, 1469 (2001).
 [25] T. S. Yu, E. Lauga, and A. E. Hosoi, Phys. Fluids **18**, 091701 (2006).
 [26] M. Manghi, X. Schlagberger, and R. R. Netz, Phys. Rev. Lett. **96**, 068101 (2006).
 [27] E. Lauga, Phys. Rev. E **75**, 041916 (2007).
 [28] B. Qian, T. R. Powers, and K. S. Breuer, Phys. Rev. Lett. **100**, 078101 (2008).
 [29] R. Dreyfus, J. Bradry, M. L. Roper, M. Fermigier, H. A. Stone, and J. Bibette, Nature (London) **437**, 862 (2005).
 [30] E. Gauger and H. Stark, Phys. Rev. E **74**, 021907 (2006).
 [31] H. Berg, *E. Coli in Motion* (Springer-Verlag, New York, 2004).
 [32] L. Turner, W. S. Ryu, and H. C. Berg, J. Bacteriol. **182**, 2793 (2000).
 [33] H. C. Berg, Phys. Today **53** (1), 24 (2000).
 [34] R. Thar and T. Fenchel, Appl. Environ. Microbiol. **71**, 3682 (2005).
 [35] M. Kanbe, J. Yagasaki, S. Zehner, M. Göttfert, and S. Aizawa, J. Bacteriol. **189**, 1083 (2007).
 [36] J. P. Armitage, T. P. Pitta, M. A.-S. Vigeant, H. L. Packer, and R. M. Ford, J. Bacteriol. **181**, 4825 (1999).
 [37] T. Fenchel and R. Thar, FEMS Microbiol. Ecol. **48**, 231 (2004).
 [38] Y. Magariyama, S. Masuda, Y. Takano, T. Ohtani, and S. Kudo, FEMS Microbiol. Lett. **205**, 343 (2001).
 [39] J. Lighthill, J. Eng. Math. **30**, 35 (1996).
 [40] K. Namba and F. Vonderviszt, Q. Rev. Biophys. **30**, 1 (1997).
 [41] T. Mignot, Cell. Mol. Life Sci. **64**, 2733 (2007).
 [42] M. Miyata, Trends Microbiol. **16**, 6 (2008).
 [43] S. L. Bardy, S. Y. M. Ng, and K. F. Jarrell, Microbiology **149**,

- 295 (2003).
- [44] D. Kaiser, *Curr. Biol.* **10**, R777 (2000).
- [45] C. Wolgemuth, E. Hoiczky, D. Kaiser, and G. Oster, *Curr. Biol.* **12**, 369 (2002).
- [46] M. Miyata, W. S. Ryu, and H. C. Berg, *J. Bacteriol.* **184**, 1827 (2002).
- [47] J.-F. Joanny, F. Jülicher, and J. Prost, *Phys. Rev. Lett.* **90**, 168102 (2003).
- [48] D. A. Fletcher and J. A. Theriot, *Phys. Biol.* **1**, T1 (2004).
- [49] R. E. Davis and J. F. Worley, *Phytopathology* **63**, 403 (1973).
- [50] J. B. Waterbury, J. M. Willey, D. G. Franks, F. W. Valois, and S. W. Watson, *Science* **230**, 74 (1985).
- [51] S. Trachtenberg and R. Gilad, *Mol. Microbiol.* **41**, 827 (2001).
- [52] R. Gilad, A. Porat, and S. Trachtenberg, *Mol. Microbiol.* **47**, 657 (2003).
- [53] S. Trachtenberg, *J. Mol. Microbiol. Biotechnol.* **11**, 265 (2006).
- [54] J. Kürner, A. S. Frangakis, and W. Baumeister, *Science* **307**, 436 (2005).
- [55] S. Trachtenberg, L. M. Dorward, V. V. Speransky, H. Jaffe, S. B. Andrews, and R. D. Leapman, *J. Mol. Biol.* **378**, 778 (2008).
- [56] C. W. Wolgemuth, O. Igoshin, and G. Oster, *Biophys. J.* **85**, 828 (2003).
- [57] J. W. Shaevitz, J. Y. Lee, and D. A. Fletcher, *Cell* **122**, 941 (2005).
- [58] M. J. Daniels, J. M. Longland, and J. Gilbert, *J. Gen. Microbiol.* **118**, 429 (1980).
- [59] M. J. Daniels and J. M. Longland, *Curr. Microbiol.* **10**, 191 (1984).
- [60] R. G. Cox, *J. Fluid Mech.* **44**, 791 (1970).
- [61] J. B. Keller and S. I. Rubinow, *J. Fluid Mech.* **75**, 705 (1976).
- [62] S. Nakamura, Y. Adachi, T. Goto, and Y. Magariayama, *Biophys. J.* **90**, 3019 (2006).
- [63] W. R. Schneider and R. N. Doetsch, *J. Bacteriol.* **117**, 696 (1974).
- [64] G. E. Kaiser and R. N. Doetsch, *Nature (London)* **255**, 656 (1975).
- [65] H. C. Berg and L. Turner, *Nature (London)* **278**, 349 (1979).
- [66] Y. Magariyama and S. Kudo, *Biophys. J.* **83**, 733 (2002).
- [67] H. Wada and R. R. Netz, *Phys. Rev. Lett.* **99**, 108102 (2007).
- [68] L. D. Landau and E. M. Lifshitz, *Theory of Elasticity* (Butterworth Heinemann, Boston, 1986).
- [69] H. Hotani, *J. Mol. Biol.* **106**, 151 (1976).
- [70] R. E. Goldstein, A. Goriely, G. Huber, and C. W. Wolgemuth, *Phys. Rev. Lett.* **84**, 1631 (2000).
- [71] G. Chirico and J. Langowski, *Biopolymers* **34**, 415 (1994).
- [72] G. Chirico, *Biopolymers* **38**, 801 (1996).
- [73] H. Wada and R. R. Netz, *Europhys. Lett.* **77**, 68001 (2007).
- [74] D. L. Ermak and J. A. McCammon, *J. Chem. Phys.* **69**, 1352 (1978).
- [75] J. Rotne and S. Prager, *J. Chem. Phys.* **50**, 4831 (1969).
- [76] R. G. Larson, *J. Rheol.* **49**, 1 (2005).
- [77] J. Happel and H. Brenner, *Low Reynolds Number Hydrodynamics* (Noordhoff, Leyden, 1973).
- [78] G. K. Batchelor, *An Introduction to Fluid Dynamics* (Cambridge University Press, New York, 1967).
- [79] S. Chattopadhyay, R. Moldovan, C. Yeung, and X. L. Wu, *Proc. Natl. Acad. Sci. U.S.A.* **103**, 13712 (2006).
- [80] M. Doi and S. F. Edwards, *The Theory of Polymer Dynamics* (Oxford University Press, New York, 1986).
- [81] J. Yang, C. W. Wolgemuth, and G. Huber, *Phys. Rev. Lett.* **102**, 218102 (2009).
- [82] T. K. Chaudhury, *J. Fluid Mech.* **95**, 189 (1979).
- [83] E. Lauga, *Phys. Fluids* **19**, 083104 (2007).
- [84] H. C. Fu, C. W. Wolgemuth, and T. R. Powers, *Phys. Rev. E* **78**, 041913 (2008).
- [85] N. C. Darnton, L. Turner, S. Rojevsky, and H. C. Berg, *J. Bacteriol.* **189**, 1756 (2007).
- [86] R. M. Macnab and M. K. Ornston, *J. Mol. Biol.* **112**, 1 (1977).
- [87] D. Coombs, G. Huber, J. O. Kessler, and R. E. Goldstein, *Phys. Rev. Lett.* **89**, 118102 (2002).
- [88] H. Wada and R. R. Netz, *Europhys. Lett.* **82**, 28001 (2008).
- [89] M. Ishimaru, T. Toyota, K. Takakura, T. Sugawara, and Y. Sugawara, *Chem. Lett.* **34**, 46 (2005).
- [90] A. Goriely and M. Tabor, *Nonlinear Dyn.* **21**, 101 (2000).
- [91] S. V. Panyukov and Y. Rabin, *Phys. Rev. E* **62**, 7135 (2000).
- [92] S. Allison, R. Austin, and M. Hogan, *J. Chem. Phys.* **90**, 3843 (1989).
- [93] A. J. Spakowitz and Z.-G. Wang, *Biophys. J.* **88**, 3912 (2005).
- [94] R. E. Goldstein, T. R. Powers, and C. H. Wiggins, *Phys. Rev. Lett.* **80**, 5232 (1998).